

The University of Maine

DigitalCommons@UMaine

Electronic Theses and Dissertations

Fogler Library

Spring 5-6-2022

Joining Methods For Continuous Fiber Reinforced Thermoplastic Composites In Structural Applications

Andrew Moran

University of Maine, andrew.r.moran@maine.edu

Follow this and additional works at: <https://digitalcommons.library.umaine.edu/etd>



Part of the [Applied Mechanics Commons](#), and the [Structural Engineering Commons](#)

Recommended Citation

Moran, Andrew, "Joining Methods For Continuous Fiber Reinforced Thermoplastic Composites In Structural Applications" (2022). *Electronic Theses and Dissertations*. 3559.

<https://digitalcommons.library.umaine.edu/etd/3559>

This Open-Access Thesis is brought to you for free and open access by DigitalCommons@UMaine. It has been accepted for inclusion in Electronic Theses and Dissertations by an authorized administrator of DigitalCommons@UMaine. For more information, please contact um.library.technical.services@maine.edu.

**JOINING METHODS FOR CONTINUOUS FIBER REINFORCED THERMOPLASTIC
COMPOSITES IN STRUCTURAL APPLICATIONS**

By

Andrew Moran

B.S. University of Maine, 2019

A THESIS

Submitted in Partial Fulfillment of the

Requirements for the Degree of

Master of Science

(in Mechanical Engineering)

The Graduate School

The University of Maine

May 2022

Advisory Committee:

Dr. Roberto Lopez-Anido, Professor of Civil Engineering, Advisor

Dr. Keith Berube, Associate Professor of Mechanical Engineering Technology

Dr. Senthil Vel, Professor of Mechanical Engineering

Dr. Robert Hart, Mechanical Engineer, Materials Application & Integration, GVSC

© 2022 Andrew Moran

All Rights Reserved

JOINING METHODS FOR CONTINUOUS FIBER REINFORCED THERMOPLASTIC COMPOSITES IN STRUCTURAL APPLICATIONS

By: Andrew Moran

Thesis Advisor: Dr. Roberto Lopez-Anido

An Abstract of the Thesis Presented
In Partial Fulfilment of the Requirements of the
Degree of Master of Science
In Mechanical Engineering
May 2022

Continuous fiber reinforced thermoplastic (CFRTP) composites have been proposed as an alternative to metals in structural applications. CFRTP composites can be used to create structures that are lighter weight, have better resistance to environmental factors, and have the potential to be recycled. However, one of the main challenges to CFRTP composites is connections between structural members. The goal of this thesis is to investigate the feasibility of joining CFRTP composites to both similar and dissimilar materials through literature review, coupon testing, design of a structural joint, and a small scale laboratory prototype of the joint. To achieve this goal the following steps were implemented.

- 1) Conduct a literature review to determine the state of the art in joining methods, optimal thermoplastic materials to use, and appropriate computer modeling techniques for joints.
- 2) Perform coupon level testing to obtain standard mechanical properties of the thermoplastic materials, and to characterize material joining methods.

- 3) Design a structural CFRTP composite joint.
- 4) Test a small scale prototype of the joint for design validation.

Two joining methods were selected to be examined: adhesive bonding and mechanical fastening. Carbon fiber-Polyphenylene sulfide (PPS) unidirectional composite tape was selected to consolidate plates with quasi-isotropic layups. Lap shear joints were examined using experimental evaluations. The experiments serve to characterize the mechanical properties required for structural design using the proposed joining methods: adhesive bonding strength and fastener bearing strength. In addition, a comprehensive program of standard tests for material characterization of the CFRTP composite were conducted to generate properties for structural analysis. A structural model of a connection in a bridging structure was developed using finite element analysis. Lastly, a prototype of the joint was constructed and tested.

DEDICATION

This thesis is dedicated to my parents who have supported me throughout my entire life.

ACKNOWLEDGEMENTS

There are so many people that have assisted me throughout my entire degree process. I would first like to thank Dr. Roberto Lopez-Anido for offering me the position to work on this project, as well as being my advisor. Your help has been instrumental in navigating the past 3 years of grad school and your support has been crucial to my success.

I would also like to thank the other GVSC leadership team members. David, your guidance and insight during some of the challenging times that occurred during this project has been invaluable. I knew that you were always there to support me and you provided the resources I needed to complete the task. Beckry, it has been a great pleasure to work with you and the highlight has to be sharing an office with you for a summer. Your insight into composite materials greatly helped me, especially in the beginning of my studies. Keith, your assistance during testing was pivotal in moving the project forward. Your wealth of knowledge and attention to detail greatly helped me. Jon, your management was extremely helpful in orchestrating materials and laboratory equipment that I needed.

From the initial summer in the lab to the final winter, Danny and Bill, you have always been there to give me a hand and share your expertise in thermoplastic consolidations. Thank you for all the work that you did for me and the beautiful specimens and plates you produced. I always appreciated our little conversations while we waited for a consolidation to finish.

I would also like to thank the entire lab operations crew, led by Chris Urquhart, for their assistance in setting up and running my testing. There are so many people that I have come in contact with at the composite center that are always willing to help out in any way they can and it is greatly appreciated.

Outside of work I have to thank MJ and JP for their support during my masters. It was always nice to have someone outside of engineering to talk and vent to about the problems that may have been occurring in the lab. Your support helped to make the almost 3 years fly by and I am so appreciative of your friendship.

To my family, thank you so much for supporting me throughout this entire process. I know that this took longer than expected, but you have always had my back and have always been supportive of my degree.

Finally, to my girlfriend Roxanne. We met as I was starting this process in 2019 and after that summer have been physically separated because of it. We have made a long distance relationship work and I feel that we are closer for it. But, as the door closes on this degree, another one opens for a life with you. Thank you for your support and motivation to complete this degree. I love you and look forward to where life takes us.

TABLE OF CONTENTS

DEDICATION	iii
ACKNOWLEDGEMENTS	iv
LIST OF FIGURES	x
LIST OF TABLES	xiv
LIST OF EQUATIONS	xvi
CHAPTER 1: INTRODUCTION	1
1.1 Project Background	1
1.2 Purpose of the Research	2
1.3 Thesis Organization.....	3
CHAPTER 2: MATERIAL SELECTION AND MANUFACTURING	4
2.1 Fiber Reinforced Thermoplastic Selection.....	4
2.1.1 Advantages of Thermoplastic Composites	4
2.1.2 Exploration of Thermoplastic Composites Matrices	6
2.1.3 Exploration of Continuous Fiber Reinforcement for Thermoplastics	9
2.2 Manufacturing Methods	11
2.2.1 Processing Parameters Based on Crystallinity.....	11
2.2.2 Tape Layup	13

2.2.3	Consolidation Utilizing a Closed Mold Under Vacuum.....	15
2.2.4	Consolidation Using a Closed Mold Without Vacuum	20
2.3	Conclusion.....	21
CHAPTER 3: MATERIAL CHARACTERIZATION		23
3.1	Introduction	23
3.2	Bearing Testing	27
3.2.1	Bearing Results	29
3.3	Adhesive Testing.....	33
3.3.1	Surface Preparation.....	35
3.3.2	Adhesive Joint Preparation	38
3.3.3	Adhesive Results.....	39
3.4	Additional Properties.....	41
3.5	Conclusions	42
CHAPTER 4: COMPOSITE BEAM JOINT Prototype		44
4.1	Introduction	44
4.1.1	Load Definition.....	45
4.2	Laminate Analysis.....	47
4.2.1	Timoshenko Beam Assumption.....	50
4.3	Design Theory	53

4.4	FEA Modeling.....	55
4.4.1	Full Scale Model.....	57
4.4.2	Prototype Scale Model.....	64
4.5	Prototype Beam Section Manufacturing	66
4.5.1	Truncated Hinge.....	66
4.5.2	Panel Fabrication	69
4.5.3	Aluminum Section Processing.....	73
4.5.4	Assembly.....	74
4.5.5	DIC Setup.....	76
4.6	Testing.....	78
4.6.1	Initial Mechanical Testing	78
4.6.2	Temperature Cycling	82
4.6.3	Secondary Mechanical Testing.....	85
4.7	Discussion of Experimental Results.....	86
4.8	Conclusion and Recommendations	91
CHAPTER 5: CONCLUSION AND RECOMMENDATIONS		94
5.1	Conclusions	94
5.2	Recommendations for Future Work.....	96
5.2.1	Scalability	96

5.2.2	Optimization/modeling	98
5.2.3	Hybrid laminates	99
5.2.4	Full Scale Structural Beam	99
APPENDIX A.....		106
APPENDIX B.....		110
BIOGRAPHY OF THE AUTHOR.....		117

LIST OF FIGURES

Figure 1. Classification of thermoplastic matrices. Source: [13].....	7
Figure 2: DSC graph for GF/PP	12
Figure 3: 50 mm wide CFRTP composite tape.....	13
Figure 4: Fiber Forge Relay 2000 automated tape layup machine	15
Figure 5: Aluminum vacuum mold.....	16
Figure 6: Vacuum mold under hydraulic press.....	17
Figure 7: Consolidation temperature and pressure for CF/PPS	17
Figure 8: Defect composite plate with air bubbles and cracks	19
Figure 9: Steel consolidation mold	20
Figure 10: Consolidated CF/PPS plate	21
Figure 11: Hi-Lok fastener.....	28
Figure 12: Typical bearing specimen with painted DIC pattern.....	29
Figure 13: Typical bearing test specimen after testing viewed from the side that was in contact with the (a) nut (b) interior surface.	30
Figure 14: Front view of bearing damage.....	30

Figure 15: Single-shear bearing stress-strain curves representing typical samples from each material	33
Figure 16: Plasma treatment of specimen.....	36
Figure 17: Untreated CF/PPS surface	37
Figure 18: Plasma treated CF/PPS surface	37
Figure 19: Effect of plasma treatment time on surface free energy.....	37
Figure 20: Adhesive 1 bond line.....	39
Figure 21: Failed Adhesive 1 Specimen	40
Figure 22: Failed Adhesive 2 Specimen	40
Figure 23: T-style aluminum connector.....	54
Figure 24: L-style aluminum connector.....	54
Figure 25: Simple FEA full scale beam	58
Figure 26: Full FEA beam loading	59
Figure 27: Deflections of simple FEA full beam.....	60
Figure 28: ½ full length FEA model.....	61
Figure 29: Displacement field of ½ full bridge structure.....	62

Figure 30: Through thickness scaling factor graph.....	63
Figure 31: Stress concentration at bolts	63
Figure 32: Prototype FEA model.....	65
Figure 33: Prototype FEA displacement.....	66
Figure 34: Truncated hinge	67
Figure 35: Steel replacement for truncated hinge	69
Figure 36: Bottom flange in consolidation press	71
Figure 37: Press temperature cycle	72
Figure 38: Flange fiber squeeze out.....	72
Figure 39: Web panel with bolt holes	73
Figure 40: Processed aluminum members	74
Figure 41: Prototype section at various stages of assembly	75
Figure 42: Prototype being craned into test frame.....	75
Figure 43: DIC system setup.....	77
Figure 44: DIC face with point trackers	77
Figure 45: CAD model of test setup	80

Figure 46: Actual test setup	80
Figure 47: Crosshead displacement vs. load for initial 30 kN loadings	81
Figure 48: Specimen in environmental chamber	82
Figure 49: Temperature and humidity cycle	83
Figure 50: Temperature data for cycle 2.....	84
Figure 51: Humidity data for cycle 2.....	84
Figure 52: Crosshead displacement for final loading test (210 kN)	86
Figure 53: Pre and post temperature cycle comparison graph.....	87
Figure 54: Out of plane motion peak under 210 kN loading	89
Figure 55: Out of plane motion vs. load under 210 kN loading	89
Figure 56: Vertical displacements at 210 kN of load	90
Figure 57: Horizontal displacement at 210 kN of load.....	91

LIST OF TABLES

Table 1: Matrix of selected polymers with relevant properties.	8
Table 2: Fiber comparison matrix.....	10
Table 3: Set temperatures and pressures for thermoplastic materials.....	18
Table 4: Single-shear bearing results.....	32
Table 5: Mechanical properties of selected adhesives.....	33
Table 6: Experimentally determined properties for unidirectional specimens.....	42
Table 7: Experimentally determined properties for quasi-isotropic specimens.....	42
Table 8: Properties of existing aluminum members.....	45
Table 9: Acceptable beam deflections.....	46
Table 10: Strength properties of CF/PPS.....	57
Table 11: Composite layup for FEA model.....	58
Table 12: Hinge replacement decision matrix.....	68
Table 13: Prototype panel dimensions.....	70
Table 14: Prototype load stages.....	81

Table 15: Mechanical testing cross head average maximum displacement 85

Table 16: Stiffness degradation of prototype..... 88

LIST OF EQUATIONS

Equation 1: Bearing Stress (σ^{br}).....	31
Equation 2: Ultimate Bearing Strength (F^{bru}).....	31
Equation 3: Bearing Strain (ε^{br}).....	31
Equation 4: Bearing Chord Stiffness (E^{br}).....	32
Equation 5: Ultimate Adhesive Strength (F^{adh}).....	41
Equation 6: Minor Poisson's ratio (ν_{21}).....	47
Equation 7: Reduced Stiffness Matrix (Q).....	48
Equation 8: Off Axis Reduced Stiffness Matrix (Q^{bar}).....	48
Equation 9: Off Axis Reduced Stiffness Matrix term (Q_{11}).....	48
Equation 10: Off Axis Reduced Stiffness Matrix term (Q_{12}).....	48
Equation 11: Off Axis Reduced Stiffness Matrix term (Q_{16}).....	48
Equation 12: Off Axis Reduced Stiffness Matrix term (Q_{22}).....	48
Equation 13: Off Axis Reduced Stiffness Matrix term (Q_{26}).....	48
Equation 14: Off Axis Reduced Stiffness Matrix term (Q_{66}).....	48
Equation 15: Laminate Rigidity (A).....	49

Equation 16: Laminate Rigidity (B).....	49
Equation 17: Laminate Rigidity (D)	49
Equation 18: ABD matrix ($[ABD]$).....	49
Equation 19: abd matrix ($[abd]$).....	49
Equation 20: Effective Young's Modulus in the x-direction (E_x)	49
Equation 21: Effective Young's Modulus in the y-direction (E_y)	50
Equation 22: Effective Poisson's Ratio (ν_{12})	50
Equation 23: Effective Shear Modulus (G_{xy}).....	50
Equation 24: Beam Deflection under Distributed Load (δ^D_{max}).....	51
Equation 25: Beam Deflection under Point Load (δ^P_{max})	51
Equation 26: Centroid about the y-axis (y^{bar})	52
Equation 27: Second Area Moment of Inertia (I_{yy}).....	52
Equation 28: Second Area Moment of Inertia Summation (I_{yy})	52
Equation 29: Tsai-Wu failure criterion	55
Equation 30: Tsai-Wu failure coefficient (f_I)	56
Equation 31: Tsai-Wu failure coefficient (f_{II})	56

Equation 32: Tsai-Wu failure coefficient (f_2) 56

Equation 33: Tsai-Wu failure coefficient (f_{22}) 56

Equation 34: Tsai-Wu failure coefficient (f_{66}) 56

Equation 35: Axial Stiffness (k_{axial}) 68

Equation 36: Bending Stiffness (k_{bend}) 68

Equation 37: Euler Buckling (σ_b) 78

CHAPTER 1: INTRODUCTION

1.1 Project Background

The United States Army Ground Vehicle Systems Center (GVSC) has an initiative to explore the use of alternate materials in the construction of structures and vehicles.

Currently a large portion of military vehicles and structures are made of metal components. The Advanced Structures and Composites Center (ASCC) is tasked with researching the feasibility of replacing these metallic components with alternate materials that have more beneficial properties. Such benefits include light weighting of the part, increased corrosion resistance, recyclability, and ease of manufacturing. However, use of these non-traditional materials is often not as easy as just switching the material. Issues can arise in part strength, geometry, or joining methods to other parts, just to name a few. This thesis outlines the research, considerations, and design that go into developing these hybrid systems.

One of the most popular alternate materials to metal is fiber reinforced plastic parts. These composite parts are formed from a high strength fiber (like carbon, glass, or nylon) suspended in a lower strength polymer matrix. The matrix is most commonly classified as either a thermoset or a thermoplastic. A thermosetting material is one that reaches its decomposition temperature before its melt temperature, whereas a thermoplastic material reaches its melting temperature before its decomposition temperature [1]. In other words, a thermoplastic can be reheated after its initial consolidation and used again with minimal loss to its physical properties. A thermoset on the other hand cannot be reheated and used again after its initial consolidation as the material will have degraded. A full

comparison of thermoplastics and thermosets is included in Chapter 2 of this thesis.

This research was created to further understand how continuous fiber reinforced thermoplastic structures can be constructed and how they interact with existing metallic components. The study sought to investigate these interests through thermoplastic material characterization, composite structural design, and testing of a small scale prototype.

1.2 Purpose of the Research

The purpose of this research is to investigate the feasibility of developing a continuous fiber reinforced thermoplastic structure that interfaces with an existing metallic part. The design of a joining method between the thermoplastic and metallic part must be explored as research has not been conducted for structures and load levels of this magnitude. The following research objectives were identified for this study:

1. Material literature review, investigation, and selection
2. Material characterization of joining methods through standardized mechanical testing
3. Design of a CFRTP beam that interfaces with a metallic part
4. Testing and assessment of the structure and joint

1.3 Thesis Organization

This thesis is organized into five chapters as follows:

- Chapter 1: Introduction; a brief background on the project, the motivation of the research, and the goals of the study.
- Chapter 2: Material Selection and Manufacturing; the literature review and considerations that went into selecting the thermoplastic material, as well as the manufacturing process for the composite parts.
- Chapter 3: Material Characterization; the literature review of possible joining methods, followed by material testing for bolted and adhesive specimens
- Chapter 4: Composite Beam Joint Prototype; the design, construction and testing of a small scale prototype to aid in further understanding of CFRTP composite structures
- Chapter 5: Conclusion and Recommendations; a summary of the findings from this research and recommendations for future work.

CHAPTER 2: MATERIAL SELECTION AND MANUFACTURING

The first step of the design process was to explore the available materials and manufacturing methods available to the project. This chapter will present the literature review of continuous fiber reinforced thermoplastic (CFRTP) composites that was carried out. This will detail the advantages of thermoplastic composites over other materials, as well as the design space of thermoplastic composites matrices and fiber reinforcement that were examined for this project.

Following the literature review a section on manufacturing parameters will be discussed. This will include an examination into the forming process, processing parameters, and scalability of the operation.

2.1 Fiber Reinforced Thermoplastic Selection

This section will detail the research conducted that led to the selection of a thermoplastic matrix of polyphenylene sulfide (PPS) reinforced with carbon fibers (CF).

2.1.1 Advantages of Thermoplastic Composites

In general, the greatest advantage of thermoplastic composites are their high weight to strength ratio. Compared to metals, such as steel or aluminum, thermoplastic composites have the potential to provide similar strengths at a fraction of the weight [2]. This is mainly due to their low densities, created from strong fibers suspended in a thermoplastic matrix. This allows for the development of lighter structures which can improve factors such as fatigue wear, transportability, and energy efficiency [3].

Engineering and performance thermoplastic composites feature many desirable properties over thermoset composites. They can be recycled, have less of an environmental impact, have higher service temperatures, are faster to produce, have higher impact toughness, and their source materials have virtually unlimited shelf life [4].

Thermoplastic composites are also easier to manufacture than many other materials. Whereas a thermoset may require a tedious vacuum bagging and autoclave process, a thermoplastic is able to be quickly stamp formed into a final part. Additionally, thermoplastics are able to be injected molded or pultruded. All of these processes can be highly automated and lend themselves to rapid part development in few steps [5].

In terms of cost, thermoplastic composites are competitive to other materials. Cost is not limited to just raw materials, but also includes processing costs to transform the material into the final part. The relative ease of manufacturing thermoplastic composite parts compared to thermosets results in less man hours being required. Thermoplastic composites can also decrease costs by requiring less raw material to produce thinner, equally strong parts compared to traditional metallic structures [6].

In terms of joining methods, thermoplastic composites have the advantage of being able to be secondary formed and joined through methods such as welding. It was also found that thermoplastic composites show superior bolted joint performance to thermosets reinforced with the same type of fibers [7]. Concerning adhesive joining methods, thermosets and thermoplastics mainly differ in their surface preparations. While a thermoset can be prepared through an abrasion process such as grit blasting,

thermoplastic bonding is most optimized when plasma [8] or UV treatments are utilized [9].

2.1.2 Exploration of Thermoplastic Composites Matrices

As stated earlier, CFRTP composites feature fibers suspended in a thermoplastic matrix. The breadth of available thermoplastic matrices are vast, but can be divided into a few classifications. The first classification is crystallinity. Thermoplastic composites are commonly classified as amorphous or semi-crystalline based on their polymer chains. In amorphous materials the chains are arranged randomly and have no specific order or alignment. In semi-crystalline materials, the polymer chains have an order and structure in portions of the matrix [10]. The prefix “semi” denotes that some regions in a semi-crystalline structure do not develop a crystalline lattice, and instead are amorphous. The degree of crystallinity is highly dependent on how the part is processed [11], and will be discussed in more detail in Section 2.2.1.

Another common classification of thermoplastic matrices is the performance level. Polymer matrices range from commodity, to engineering, to performance. A commodity grade thermoplastic is one that is designed for mass production of a variety of objects where specific properties may not be relevant, such as flammability or chemical stability. Commodity polymers are common in single use products, such as packaging films, bottles, bags, etc. [12] and are often the cheapest. Engineering plastics are specifically designed polymers that feature increased thermal, strength or chemical properties. The highest grade of thermoplastic matrices are performance grade. These are the most

expensive thermoplastic polymers and have the highest thermal and mechanical properties. Figure 1 showcases a chart of commonly used thermoplastics and their designations in terms of crystallinity and performance.

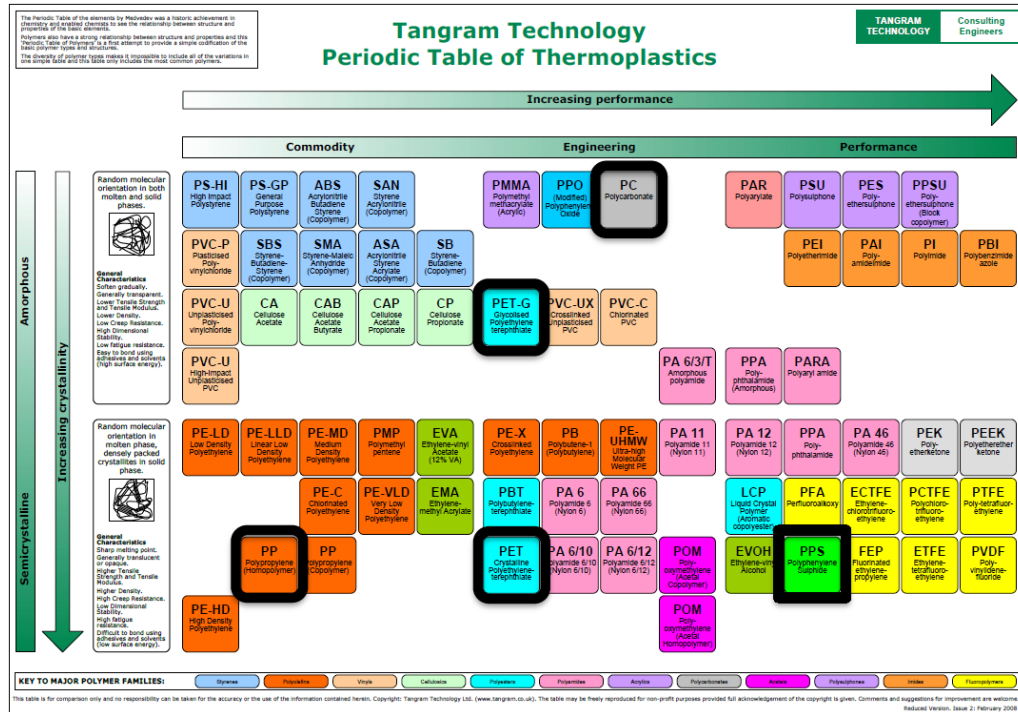
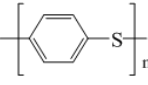
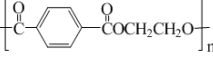
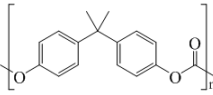
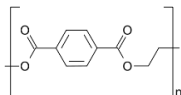



Figure 1. Classification of thermoplastic matrices. Source: [13]

Five thermoplastic polymers were selected for this project. These five polymers include: Polyethylene terephthalate glycol (PETg), Polycarbonate (PC), Polypropylene (PP), Polyethylene terephthalate (PET) and Polyphenylene sulfide (PPS). These five were selected for their vast coverage of the possible thermoplastic design space. They are commonly available from major manufacturers and feature many good properties, some of which are summarized in Table 1.

Table 1: Matrix of selected polymers with relevant properties.

Polymer	Structure	Crystallinity	Chemical Stability	Upper Use Temp. [°C]	Flame, Smoke and Toxicity
PPS		Semi-Crystalline	Very Good	200	Very Good
PET		Semi-Crystalline	Good	150	Combustible, clean smoke
PC		Amorphous	Fair	135	Good with fire retardant
PETg		Amorphous	Good	150	Good
PP		Semi-Crystalline	Fair	85	Good

With the design space narrowed down to these five thermoplastic materials at a project level, a selection could now be made for this specific task. PPS was selected as the material of interest due to its high strength, high temperature stability, and its very good fire resistance. Polyphenylene sulfide is a widely used high performance plastic. It consists of aromatic rings linked by sulfur atoms [14]. It has very good fatigue properties due to good fiber-matrix adhesion, leading to minor progressive damage under loading [15]. PPS has been used in many industries including aerospace [16] [17].

2.1.3 Exploration of Continuous Fiber Reinforcement for Thermoplastics

In addition to the selection of a thermoplastic matrix, the fiber reinforcement for the thermoplastic composite must also be specified. There are many forms of fibers that are used in thermoplastic composites, but the most common are glass (GF), carbon (CF), basalt (BF) and aramid (AF).

Glass fibers are the most widely used fibers for basic structural applications, accounting for more than 95% of fiber reinforcements. They are advantageous due to their low cost and high strength. They are nonconductive and corrosion resistant. Their biggest detractor is that they are fairly dense, limiting their applications for light weight structures. Additionally, glass fibers often have poor adherence to thermoplastic materials, leading to the fibers having to be sized. Sizing is the process of coating the fibers with an organic material to improve adherence to the matrix material, as well as protect and align the fibers [18].

Carbon fibers are the predominant high strength, high modulus fibers used in weight sensitive structures. While their cost is much greater than glass, there has also been an increase in demand for carbon fibers, which has led to a drop in price. As with glass fibers, carbon fibers are sized and/or chemically/mechanically modified to provide better adhesion to the thermoplastic matrix [19].

Basalt and Aramid fibers are less common fibers, especially for thermoplastic tapes.

Aramid fibers are polymer-based and feature high tensile strength and modulus. They also have a density that is less than carbon or glass. However, these fibers have relatively

low adhesion to thermoplastic matrices, which has delayed their adoption. Research is currently being performed on way to increase the matrix-fiber adhesion [20]. Basalt fibers are desirable because they are created from a one-stage process. Crushed basalt rock is washed and heated to 1500 °C, then extruded into fiber strands. These fibers exhibit a high modulus and strength, three times that of steel [21]. Basalt fibers are also incombustible, chemically inert, and environmentally and ecologically harmless. However, they have not had the same mass adoption as carbon or glass fibers due to lesser strength properties [22].

Table 2 features a comparison of properties for each fiber, ranking them from lowest to highest in terms of density, ultimate strength, and cost. This information was compiled by Christoph Unterqeger et al. [23].

Table 2: Fiber comparison matrix

	Density	Strength	Cost
Lowest	AF	BF	GF
	CF	AF	BF
Highest	GF	GF	CF
	BF	CF	AF

Ultimately, carbon fiber was selected as the fiber of interest for this research. The required strength to weight ratio limited the design space to carbon or aramid fibers. Taking into account relative cost and industry availability it was determined that carbon fiber reinforcement would be the best selection.

2.2 Manufacturing Methods

An iterative process was used to determine optimal processing parameters and methods for generating CFRTP composite panels. For ease of manufacturing, and based on available laboratory equipment, it was determined that CFRTP tapes would be used. These tapes contain continuous fibers suspended in the matrix material. They arrive in rolls of varying widths and sizes. The tapes are cut and stacked to the desired thickness and ply orientation to form a composite blank. They are then consolidated using a heated press. Two different consolidation molds were investigated to reduce voids forming in the part.

2.2.1 Processing Parameters Based on Crystallinity

To be able to consolidate the composite panels temperature properties of the thermoplastic matrices must be known. As seen in Figure 1 in Section 2.1.2 thermoplastic composite matrices are commonly divided into two crystallinity classes; amorphous and semi-crystalline. These classifications designate how the material must be consolidated. During consolidation both materials are heated above their melt temperatures to allow free flow of the polymer matrix, then cooled. For semi-crystalline material the cooling rate must be controlled between the melt temperature and the crystallization temperature, to allow for the formation of the semi-crystalline polymer structure. Too little cooling time could result in a lack of crystallinity, leading to decreased materials properties such as strength [24]. To determine the crystallization temperature a differential scanning calorimeter (DSC) was used.

DSC is a process that measures temperature and heat flows of a specimen as it is heated or cooled. By observing the peaks in heat flow the melt and crystallization temperature of the material can be determined. The DSC work for this project was completed at Winona State University using a DSC TA Q100. Testing was done on all semi-crystalline materials of interest as outlined in Section 2.1.2. Figure 2 shows a typical DSC curve. As seen in the figure the material starts at room temperature and is initially heated. As the material approaches its melt temperature the energy required to raise the material by one degree increases and a peak forms. This peak is considered the melt temperature as more energy is required as the material changes phases. Once the transition is completed the endothermic reaction returns to its normal heat flow level. Next the material is cooled. Upon cooling a peak is seen in the exothermic reaction. This signifies the transition of the material back into a solid, thus locking polymer structure. As seen in the figure this process is repeatable.

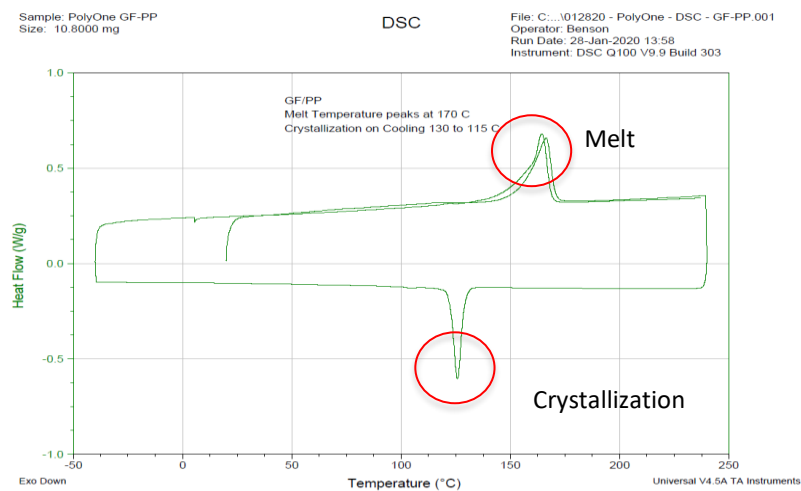


Figure 2: DSC graph for GF/PP

From these graphs the melt and crystallization temperatures could be determined for the materials of interest and are summarized in Table 3 in Section 2.2.3.

2.2.2 Tape Layup

To consolidate a thermoplastic composite part using unidirectional tapes, a layup must be made. A composite layup consists of layering multiple composite tapes to achieve the desired thickness and size of the final part. This non-consolidated layup is often called a blank. Figure 3 shows a typical 50 mm wide composite tape. Tapes can come in varying widths, typically from 25 mm to 300 mm.



Figure 3: 50 mm wide CFRTP composite tape

Two layup techniques were used during this project. The first is a hand layup. A hand layup involves cutting out and assembling the plies by hand. This is most useful in

unidirectional parts, where all of the fibers are oriented in the same direction. This is also convenient for layups where the tape width exceeds the desired blank width as the tapes can be cut to the final dimension, negating seams in the part. A seam is where two composite tapes sit next to each other in the same ply, and can lead to voids.

For more complex geometries an automated fiber placement process is preferred. The Advanced Structures and Composites Center (ASCC) houses a Fiber Forge Relay 2000 automated tape layup machine by Dieffenbacher in its Alford Advanced Manufacturing Laboratory for Structural Thermoplastics. This machine, seen in Figure 4, automatically assembles the composite blank as specified by the user. First, a roll of thermoplastic tape ranging from 50 to 150 mm is loaded onto the material creel. The tape is then fed into the machine where it is automatically cut and set onto the construction surface. The construction surface is able to translate and rotate to match the desired fiber placement and alignment. A set of friction welders then tack weld small sections of the blank to provide enough structural rigidity to transfer the part into the consolidation press. During construction of the blank the automated tape layup machine is programmed to stagger seams between layers to decrease the chance of voids forming in the part.

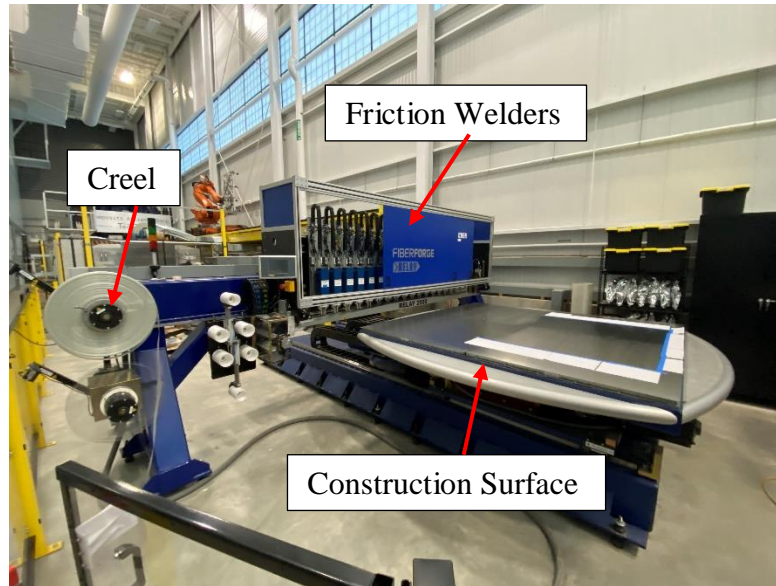


Figure 4: Fiber Forge Relay 2000 automated tape layup machine

After being laid up, either by hand or automation, the composite blank is then trimmed to final dimensions if necessary. This completes the layup step and the blank is then transferred to the consolidation step.

2.2.3 Consolidation Utilizing a Closed Mold Under Vacuum

To prevent void formation due to trapped air during the consolidation process a closed mold with a vacuum port was designed for use. The mold is made from aluminum and has two halves; a top plug and a bottom cavity. A threaded port was added to bottom half to allow for the attachment of a vacuum line. To seal the gap between the upper and lower halves of the mold a channel was fabricated into the top portion of the mold to allow for a rubber gasket to be inserted. A picture of the mold is shown below in Figure 5.

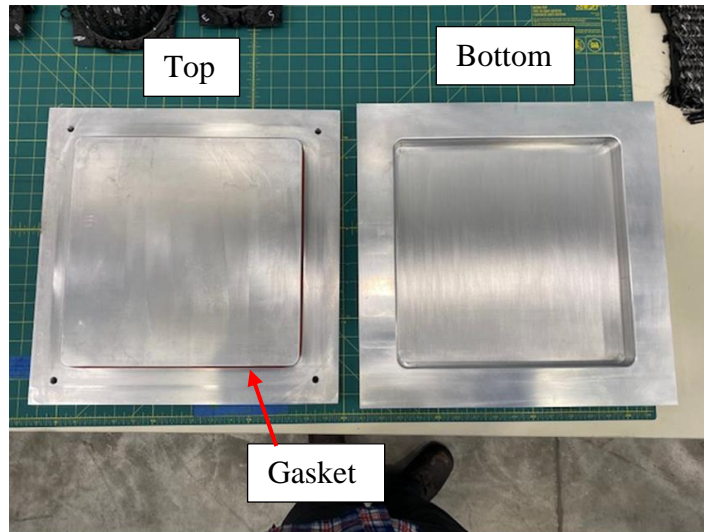


Figure 5: Aluminum vacuum mold

The consolidation process involves coating the mold surfaces in chemlease to prevent the composite from adhering to the metal. The composite blank is then inserted into the mold. The top plug is prepared with a high temperature silicone gasket lubricated with avocado oil. The mold is sealed and placed on top of a heated platen. The vacuum line is attached to the mold, fiber glass insulation is placed around the mold to prevent heat loss, and light pressure is applied from the 500 kN hydraulic press. Figure 6 shows the mold consolidation setup.

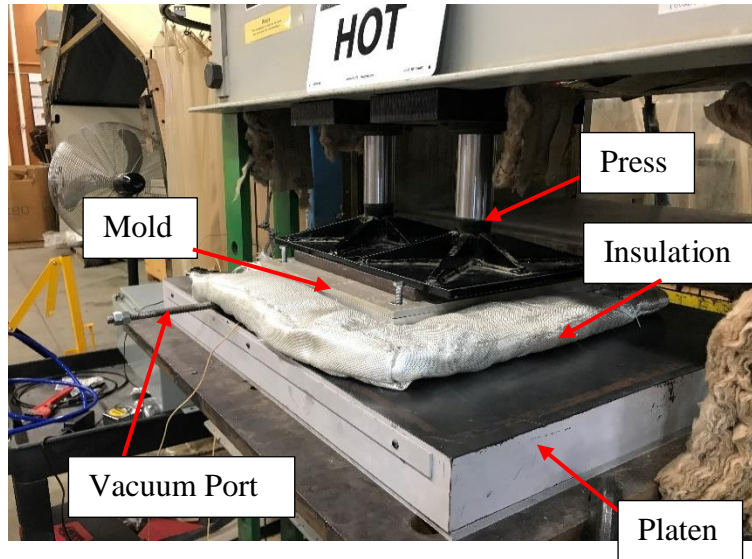


Figure 6: Vacuum mold under hydraulic press

The consolidation process involves varying temperature and pressure on the blank to create a consolidated part. Using data from the manufacturers and DMA testing results material specific consolidation curves were created. An example curve is seen in Figure 7. All materials follow a similar pressure and temperature curve.

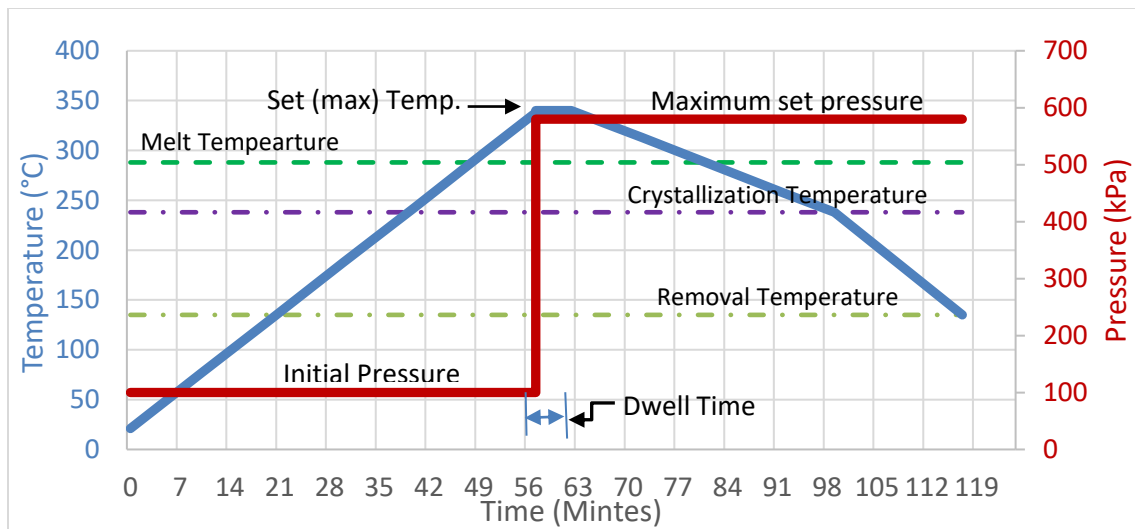


Figure 7: Consolidation temperature and pressure for CF/PPS

The material is heated under low pressure and vacuum. Once the material reaches the set temperature the pressure is increased and the vacuum port is removed and the hole is plugged. A dwell time is held to allow the viscous material to flow and combine. The material is cooled while the pressure is maintained using water and/or air cooling. For semi-crystalline materials the cooling rate is controlled until the crystallization temperature is reached, then cooled rapidly. For amorphous materials the mold is cooled as quickly as possible. Additional material set temperatures and pressures are summarized in Table 3.

Table 3: Set temperatures and pressures for thermoplastic materials

Material	Initial Pressure (psi)	Tg °C (°F)	Set Temp. °C (°F)	Set Pressure (psi)	Dwell Time (Min)	Cooling Rate °C/Min	Crystalln. Temp. °C (°F)	Removal Temp. °C (°F)
CF/PPS	15	90 (194)	340 (645)	84	5	5 (9)	210 (410)	135 (275)
GF/PPS	15	90 (194)	340 (645)	84	5	5 (9)	210 (410)	135 (275)
GF/PET	15	80 (176)	290 (555)	84	2	5 (9)	160 (320)	65 (150)
GF/PC	15	150 (302)	240 (465)	28	3	15 (27)	-	37 (100)
GF/PETg	15	90 (194)	240(465)	28	2	15 (27)	-	37 (100)
GF/PP	15	130 (266)	174 (345)	28	2	5 (9)	110 (130)	52 (125)

While this process was used to produce many panels, multiple issues arose. First, some materials with high melt temperatures, like PPS and PET, were hard to process using the

heated platen as only one side of the mold was in contact with the platen. This resulted in uneven heat distribution in the mold and created panels that were burnt on the bottom and under consolidated on the top. Secondly, the thermal expansion of aluminum (21×10^{-6} m/(m °C)) [25] is much less than that of most of the polymers. This resulted in many plates getting stuck to the lid of the mold as resin would seep onto the lid as the mold was heated, then cool and lock itself onto the lid. Additionally, other plates would become lodged in the bottom of the mold after consolidation due to the lack of a draft angle in the mold. To remove plates from either of these scenarios the plates would commonly crack as seen in Figure 8.

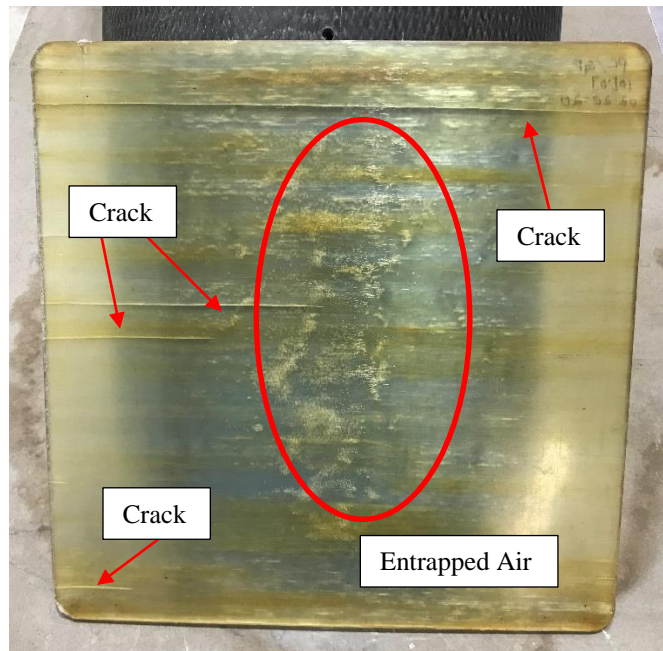


Figure 8: Defect composite plate with air bubbles and cracks

Lastly, issues were observed with the vacuum seal. The vacuum port would clog with resin, the gasket would not seal, and the aluminum threads for the vacuum line degraded and leaked. Also, the panels consolidated with or without vacuum did not show any

difference in terms of trapped air bubbles. Due to all these issues a revised mold and process was created that would not utilize a vacuum.

2.2.4 Consolidation Using a Closed Mold Without Vacuum

Utilizing the knowledge gained from the first consolidation attempt a new mold was designed. This mold is made of steel instead of aluminum and features removable walls. To process a composite part, the walls are bolted to a flat bottom steel plate, the material is inserted, and then a steel plate is rested on top of the material. A photo of a half assembled mold is shown in Figure 9. Additionally, the material consolidation size of the mold was increased from 30.4 cm x 30.4 cm to 48.3 cm x 30.4 cm.

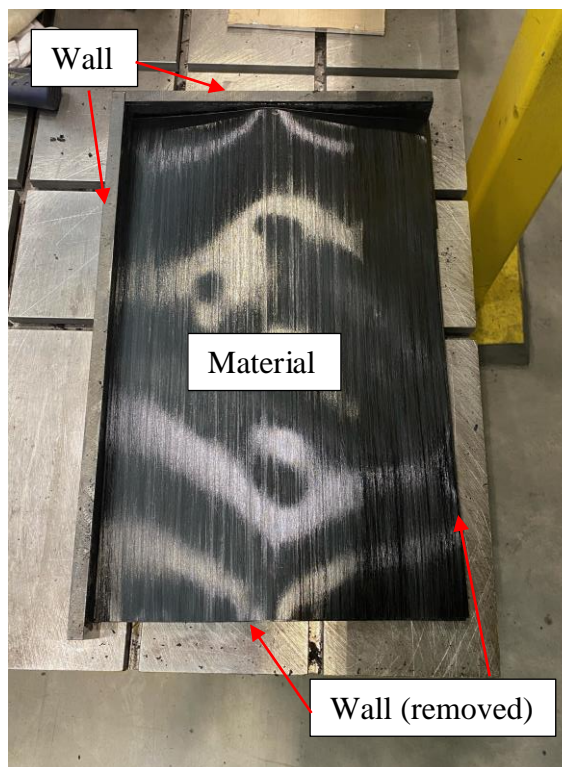


Figure 9: Steel consolidation mold

To combat issues with uneven heating, a new computer controlled press was purchased. This new press is a Monarch 100 kN hydraulic press with active heating and water cooling. This press features two temperature controlled platens that contact the top and bottom of the mold.

Utilizing the same temperature and pressures discussed in the last section, this new consolidation mold and press produce higher quality parts compared to the initial setup. The temperature is more accurately controlled, parts are easier to remove from the mold, and the parts come out with a smooth surface finish as seen in Figure 10.



Figure 10: Consolidated CF/PPS plate

2.3 Conclusion

Material selection and manufacturing were explored in this chapter. Justification for the selection of fiber reinforced thermoplastic composites over fiber reinforced thermoset

composites was presented. The breadth of thermoplastic matrices and fiber reinforcement was given and an explanation on down selection to project specific materials of carbon fiber reinforced polyphenylene sulfide (CF/PPS) was presented. Material specific properties from the manufacturers were then reported.

The iterative process of developing high quality parts was presented. This process involved determining thermal properties for each material based on crystallinity, presenting two ways to layup composites by hand, and then exploring two different mold based consolidation processes. Ultimately a mold without a vacuum port was selected and a computer controlled hydraulic consolidation press was used.

CHAPTER 3: MATERIAL CHARACTERIZATION

Upon the selection of a material of interest in Chapter 2, and an optimized manufacturing process, research could now begin on understanding the structural properties of the material. Specifically for this research there is a focus on understanding the bearing and adhesive properties. This chapter will explain the background research and testing that was accomplished to guide the development of the structural design of the task.

3.1 Introduction

Continuous fiber reinforced thermoplastic (CFRTP) composites have the potential to be used in many structural applications. However, most applications require the use of a connection or joint to attach the CFRTP part to a similar or dissimilar material.

Typically, fasteners are used as they are cheap, quick to install, easy to repair, and allow the structure to be easily disassembled. While much is known about how to design these connections in metallic structures, CFRTP's present a unique challenge as they behave differently than isotropic materials.

Bolted connections require damaging the continuous fiber architecture of the composite to bore a hole. This potentially lowers the load capacity of the composite, as well as introduces a point of stress concentration [26]. Without adequate understanding of the materials response to this bearing stress an unintended failure at the joint may occur.

Furthermore, complexity is added to the failure mode of the joint as bearing failures often feature a mix of tensile, compressive and shear failure. Bolt head off-axis rotation due single shear testing can also lead to surface damage around the bolts location. Therefore,

rigorous testing is required to characterize thermoplastic composites in bearing response to be able to utilize bolted connections.

Due to their prevalence in industry, more research has been conducted on bearing response of thermosetting composites. Xiao et al. studied the bearing strength and failure behavior of bolted thermoset composite joints [27]. They found that bearing failure occurs through a process of damage accumulation. Additionally, they observed that matrix toughness has an influence on matrix cracking and delamination. Choi et al. examined the relationship between bolt clamping force and failure load. It was found that single lap-shear bolted joints can be improved by increasing the clamping force of the fastener [28]. However, there is a limit to the improvement, typically corresponding to moderate torque, so as not to damage the fibers. Research has also been conducted on the influence of bolt-hole clearance [29]. It was found that there can be significant laminate damage variation at similar loads based on clearance size. Clearance can also effect the stiffness of the laminate, which could be critical in the design of multi-bolt structures.

While these studies have helped to characterize bearing response in thermosetting composites, fewer studies have been done for continuous fiber reinforced thermoplastic composites. Taner and Tamer investigated the load bearing performance of pin connected carbon fiber reinforced polyphenylene sulfide (CF/PPS) [30]. They investigated the variation in attainable load based on a varying edge to width and hole diameter to width ratios in double-shear pin testing. In addition, they also investigated the effect that fiber orientation had on load bearing performance. They found that pin

loading performance has a close relationship with fiber orientation of laminates and their deformation characteristics. As well, they found that the geometric parameters of end distance from the hole center, width of the plate, and pin diameter affects the load bearing performance of the composite materials. Without adequate ratios the material will fail in undesired modes (such as tension or shear-out).

More recently research has been done into enhancing the bearing strength of woven carbon fiber thermoplastic composites through additive manufacturing [31]. A novel way of tailoring the woven matrix around the hole is presented to increase the laminate's strength.

Less research has been done on adhesive bonding of thermoplastic composites due to their relatively low surface free energy. This can make achieving a structural bond difficult, and often fails in an adhesive failure at the bond surface, instead of a cohesive failure in the bond line. Additionally, thermoplastic composites are treated with mold release agents that often leave a residue on the parts surface, leading to poor bondability to the actual composite matrix and fibers [32].

To achieve a bondable surface much research has been conducted on different surface preparation techniques. Such methods include peel-ply, UV treatment and plasma treatment [33]. There are also mechanical methods such as grinding or grid blasting; however, these often yield inconsistent results and require tool wear. Due to many thermoplastics being flammable fire treatments are often not recommended.

Adhesives are typically found in three forms: single part, two part, and film based.

Single and two part adhesives arrive as liquids and are mixed and applied to the composites surface. Due to their viscosity it is sometimes hard to maintain a consistent bondline thickness. Film based adhesive solve this problem by arriving as a solid sheet. The adhesive is cut to the desired bond area and sandwiched between the two surfaces, maintaining an even bondline. Most high strength adhesives require an elevated temperature to set. Manufacturers specify the temperature, pressure, and time that the adhesive must undergo to provide the optimal bond.

There are also many different classes of adhesives that are commonly used to bond to composites. The predominantly used adhesive is epoxy based adhesives. These are preferred due to their high strength and good bondability. They also come in a wide variety of curing methods, including the ability to be cured at room temperature.

Structural acrylic based adhesives are also used as they produce high peel strengths, as well as fast cure rates. Other adhesives used include polyurethane adhesives, cyanoacrylates, and UV curable adhesives [34].

Hybrid bolted-adhesive joints have been researched [35] . However, it is found that most of the time they contribute little to increasing the joints strength. Either the adhesive or the bolt failure will dominate the overall joint failure response.

Lastly, there are other forms of composite joints that are used; however, they are outside the scope of this research. But, for a full scope of the available joint design space they will be presented. Clinching is a cold mechanical joining process where a part is pressed into another part typically with a punch and die [36]. Welding is a growing area of

interest in thermoplastic composites due to the ability of the matrix to be reheated without degradation of mechanical properties. Common welding techniques include laser assisted [37], friction spot joining [38], and friction lap joining [39]. Lastly, similar to bolted connections self-piercing rivets are used; however, they can lead to excessive fiber damage due to their self-piercing nature [40]. This is a fairly comprehensive list of available joining methods, but as thermoplastic composites become wider spread additional methods may be discovered.

For this research bolted and adhesive joints were selected as the area of interest, and mechanical tests were performed for each joining method.

3.2 Bearing Testing

Carbon Fiber Reinforced Polyphenylene Sulfide (CF/PPS) was selected as the material for this study. It is a semicrystalline performance thermoplastic that provides high strength, very good flame resistance, and a high use temperature. It was obtained from two manufactures: Toray Advanced Composites (Manufacturer A), and Celanese (Manufacturer B). The unidirectional tapes from A have a 59% fiber volume fraction (FVF), and the material from B have a 53% FVF. Full material property sheets from each manufacturer can be found in APPENDIX A.

Unidirectional tapes were obtained from the manufacturers. Tailored blanks were assembled using a fiber forge tape layup machine, using a quasi-isotropic stacking sequence of $[0/\pm 30/\pm 60/90]_s$ for material A, and $[(0/\pm 30/\pm 60/90)_2]_s$ for material B, to produce panels of similar thickness. A closed mold stamp thermoforming process was

utilized to consolidate the composite materials. The material blank was loaded into a rectangular steel mold (304.8 mm x 482.6 mm). The mold was then loaded into a computer controlled heated press with active cooling. The desired composite panel was then ejected from the mold and processed into specimens.

The composite panels were then cut to the required specimen sizes using a wet saw with a diamond tipped blade. Holes were drilled into the specimens using a solid carbide combination drill and reamer bit. Specimens were conditioned for at least 24 hours at 23 °C and 50% relative humidity before being measured and tested.

Testing was performed in accordance with ASTM D5961 Procedure B [41]. Specimens were joined using Hi-Lok HL18 steel alloy bolts and HL70 2024 T-6 collars (Figure 11). To achieve uniform bolt tightening the collars feature a shear-off head, which detach at a torque of 6.8 - 9.0 N m.



Figure 11: Hi-Lok fastener

Specimen elongation and displacements were tracked using GOM Correlate, a camera based, non-contact digital image correlation (DIC) system. The specimens' surfaces were painted with a random speckle pattern that the DIC system uses to track pixel movement using local facets. Force data and images were captured at a rate of 2 Hz using a LabVIEW program, and later processed using the calibrated DIC system. Bearing strain was calculated using the averaged displacement of five 25.4 mm long digital extensometers positioned around the bolt head.

A standard Instron 100 kN servo-hydraulic test frame with a calibrated 100 kN load cell was used. Specimens were loaded using displacement control at a speed of 1.27 mm/min. Testing concluded after a 30% drop off in load from the maximum or if the head displacement reached half the diameter of the bolt (3.18 mm).



Figure 12: Typical bearing specimen with painted DIC pattern

3.2.1 Bearing Results

Typical bearing damage was observed in all specimens. Figure 13 shows typical observed damage to the composites. Image (13.a) showcases the surface of the composite in contact with the bolt head. There is a slight depression into the material due to the torqued bolt, but damage appears to be minimal and effects only the top layer of

fiber. Image (13.b) shows damage that was observed on the interior surface where the 2 specimens are in contact with each other. Typical bearing failure is observed with the bunching of fibers at the top of the image.

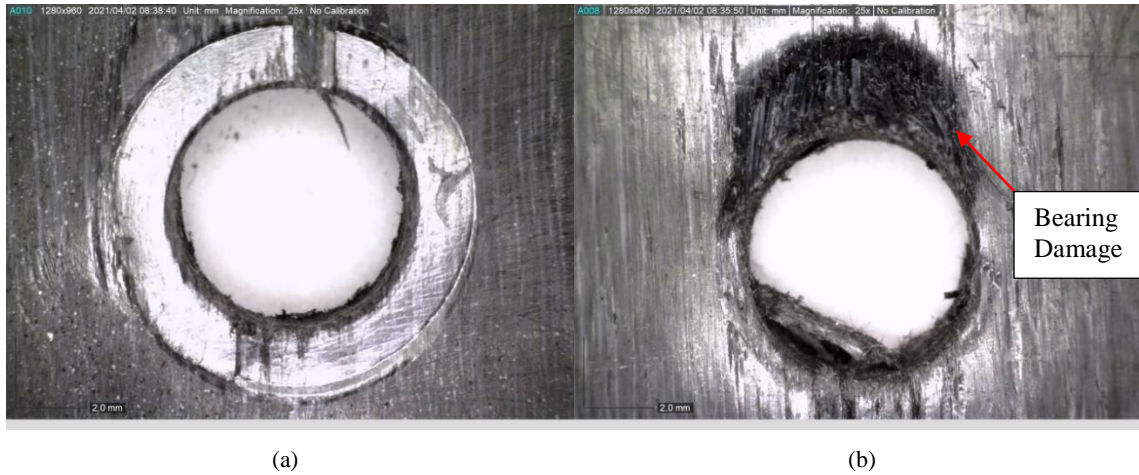


Figure 13: Typical bearing test specimen after testing viewed from the side that was in contact with the (a) nut (b) interior surface.

Due to specimen bending and bolt rotation, damage is observed on the interface surfaces between the bolt and the material. While damage to top layer of fiber was observed, minimal change in interior layers was noticed as seen in Figure 14.

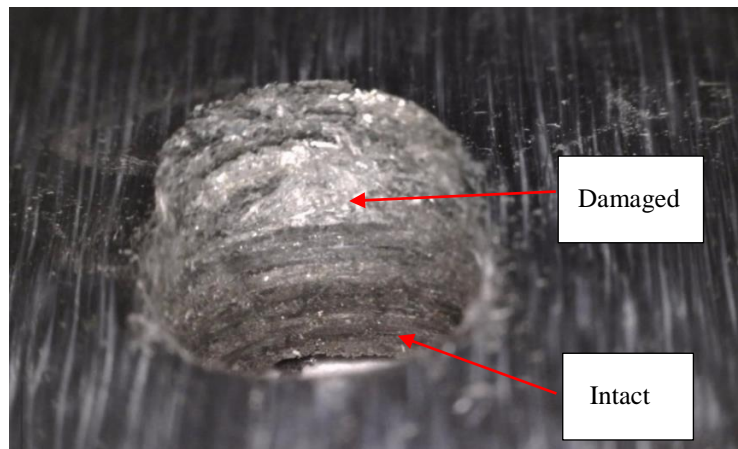


Figure 14: Front view of bearing damage

The bearing stress was calculated throughout the testing via Equation 1 as specified in the ASTM standard. A k factor of 1.0 was used as the testing consisted of a single factor.

$$\sigma_i^{br} = \frac{P_i}{k \times D \times h} \quad \text{Equation 1}$$

Where:

σ_i^{br} = bearing stress at *i*-th data point, MPa [psi]

P_i = force at *i*-th data point, N [lbf]

k = force per hole factor: 1.0 for single-fastener or pin tests and 2.0 for double-fastener tests.

D = Hole diameter, mm [in.]

h = specimen thickness, mm [in.]

Ultimate bearing strength is calculated with Equation 2. Again, a k factor of 1.0 was used.

$$F^{bru} = \frac{P^{max}}{k \times D \times h} \quad \text{Equation 2}$$

Where:

F^{bru} = ultimate bearing strength, MPa [psi]

P^{max} = maximum force prior to failure, N [lbf]

The bearing strain was computed using Equation 3. Extensometer elongation data was obtained from the DIC recording by applying five digital extensometer to the specimen.

$$\varepsilon_i^{br} = \frac{(\delta_{1i} + \delta_{2i} + \delta_{3i} + \delta_{4i} + \delta_{5i})/5}{K \times D} \quad \text{Equation 3}$$

Where:

ε_i^{br} = bearing strain, microstrain,

δ_{ji} = extensometer-*j* displacement at *i*-th data point, mm [in.],

K = 1.0 for Procedures A, C and D, 2.0 for Procedure B.

Lastly, the bearing chord modulus was calculated using Equation 4.

$$E^{br} = \Delta\sigma^{br}/\Delta\varepsilon^{br} \tag{Equation 4}$$

Where:

E^{br} = bearing chord stiffness, MPa [psi]

The strengths and stiffness of the single-shear material testing are presented in Table 4.

This data represents an average of 7 samples for each material. Bearing stiffness was taken as a linear regression between values of 1.0% - 4.0% strain for each material.

Material A has a bearing strength that is 7.5% greater than that of material B; however, material B was found to have a bearing stiffness that is 74.5% greater than material A, and a 2% offset bearing strength that is 19.5% greater than material A.

Table 4: Single-shear bearing results

Material	Bearing Stiffness [GPa] (COV)	Maximum Bearing Strength [MPa]	2% Offset Bearing Strength [MPa]
Material A	5.41 (6.07%)	573 (2.02%)	457 (3.27%)
Material B	9.44 (5.00%)	546 (2.10%)	533 (1.50%)

While bearing strength is observed to be of similar magnitude, a large variation between the bearing stiffness and 2% offset bearing strength between materials is noticed. This variation in bearing stiffness is most apparent in Figure 15, where typical stress strain curves of the materials are shown. Material B has a more defined linear region that has a sharp transition out of linearity, whereas material A has a smaller linear region that more

gradually transitions to a nonlinear curve. Additionally, due to the smaller linear section and decreased slope of material A, the corresponding 2% offset bearing strength is less for material A compared to material B. Conversely, material A reaches a greater ultimate strength than material B. While not the same, both loading paths feature typical bearing responses, including a linear region, followed by a tapering of slope due to damage propagation, a minor decrease in strength as strain continues to build, then an additional increase in strength before the test finishes.

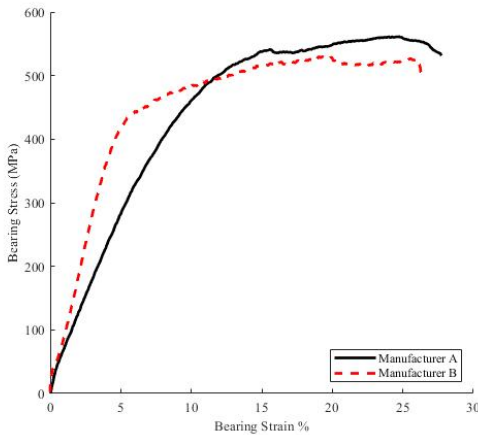


Figure 15: Single-shear bearing stress-strain curves representing typical samples from each material

3.3 Adhesive Testing

A wide range of adhesives were explored for this test, primarily focusing on ones recommended for polyphenylene sulfide. Table 5 summaries some of the many adhesives examined with relevant properties.

Table 5: Mechanical properties of selected adhesives

Adhesive	Lap Shear Strength, Al	Tensile Modulus,	Tensile Strength,	Compressive Strength,	Elongation,	Service Temp

	to Al, 23.9°C	23.9°C	23.9°C	23.9°C	23.9°C	Range
	MPa	GPa	MPa	MPa		°C
EP17HT	17.9-19.3	2.76-3.10	68.9-75.8	138-152	-	-62 to 316
SUP10HT	24.8 - 26.2	3.10 - 3.45	55.1 - 62.1	96.5-110.3	5-10%	4K to 204
SUP11HT	22.0 - 23.4	2.06 – 2.41	48.3 – 55.1	-	-	-73 to 204
EP41S-1HT	15.9-17.2	2.76-3.10	62.1-68.9	-	-	-51 to 204
EP62-1HT	13.8-15.2	3.45-3.79	68.9-75.8	-	3-5%	-51 to 232
PR-2901	45.7-46.9	-	-	-	-	-
EA 9696	33.8	-	43.4	-	-	- to 121

From this matrix of adhesives two were selected for testing. The first was SUP11HT from masterbond (Adhesive 1). This two part epoxy adhesive was desirable due to its variety of low temperature cure options (including room temperature cure) and high strength. The second adhesive selected is EA 9696 by Hysol (Adhesive 2). The main advantage of this adhesive is that it is film based, allowing for easy joining. In addition, this adhesive also has relatively high strength and features an attainable curing temperature 107 °C.

As with the bearing testing quasi-isotropic laminates were consolidated as outlined in Section 3.2. All panels were made from CF/PPS materials from manufacturer B. Coupons were cut to 25.4 mm x 101.6 mm as outlined in ASTM D5868 [42].

3.3.1 Surface Preparation

An additional step was required to prepare the CF/PPS specimens for bonding. As discussed in the introduction to this chapter, thermoplastic composites often have poor surface free energy making them hard to bond to. To increase their bondability surface treatments were applied to the specimens. From literature review it was found that plasma treatments often yield the highest increase in surface free energy when compared to UV treatments or simple wiping [33]. Plasma treatments work by arcing electricity across two electrodes. This creates plasma, a gaseous mixture of ions, radicals, electrons and neutrals. A fan located at the top of the unit head continually blows atmospheric air down onto the specimen through the arc. This creates free radicals through chain scission which form polar oxygen groups on the surface. The activated surface thus increases in free energy due to increased wettability and surface roughness [43].

A Lectro Engineering LTIII Forced Air Plasma Surface Treater was selected to apply the plasma treatment to the specimens. Exact processing parameters for CF/PPS were not specified for this machine so a study into optimal processing parameters was conducted. From literature review optimal surface free energy due to plasma treatment for PPS was found to be approximately 65-70 mN/m [33]. The plasma treater allowed for the adjustment of fan speed (0-100%), head height distance from specimen, and treatment time. Trials were conducted at fan speeds of 70% and 90% power, and treatment times ranging from 0 to 180 seconds. In all trials the head height was kept at 10 mm, as recommended by previous studies [44]. Before being treated all specimens were cleaned with isopropyl alcohol. During treatment specimens were continually moved around in

the arc to achieve an even distribution across the 25mm x 25mm treatment area. Figure 16 shows the treatment test setup.

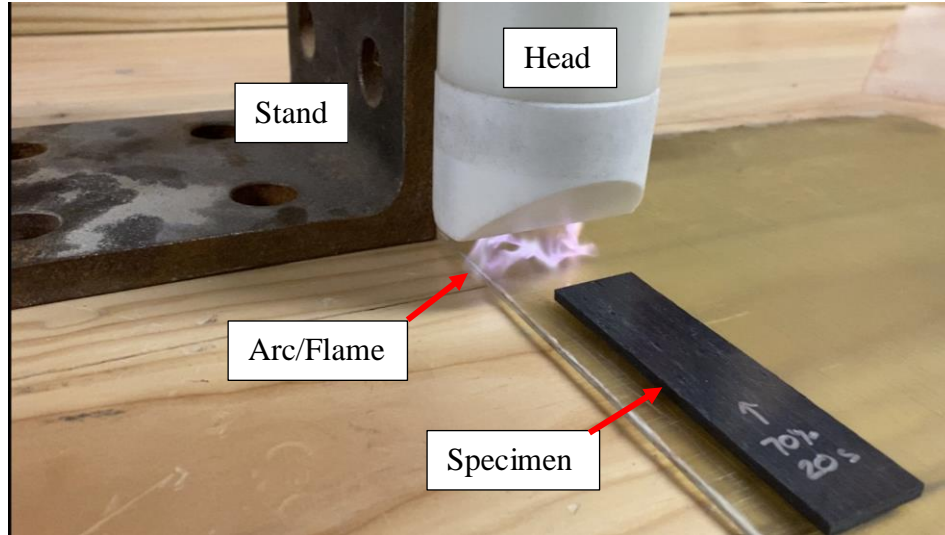


Figure 16: Plasma treatment of specimen

Upon completion of treatment surface free energy was assessed using a Kruss MSA One-Click SFE. This device dispenses two liquids to determine the wettability of the surface. The first liquid is water and the second is diiodomethane. Upon depositing the two liquids onto the surface optical cameras measure the contact angle of each droplet. Using the contact angle of each liquid the surface free energy can be determined using surface free energy analysis. An image of each droplet on an untreated surface is seen in Figure 17, and a treated surface is seen in Figure 18. The measurements were taken 10-20 times for each specimen. Averaged results of the different treatment times and power levels are summarized in Figure 19.

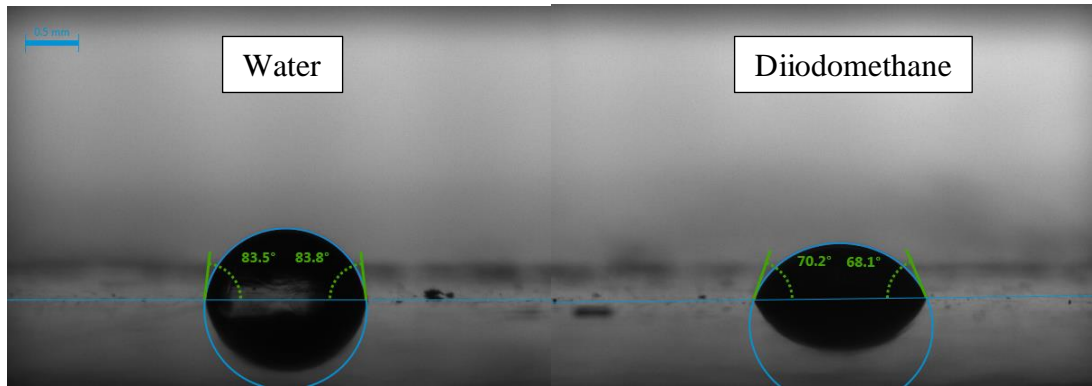


Figure 17: Untreated CF/PPS surface

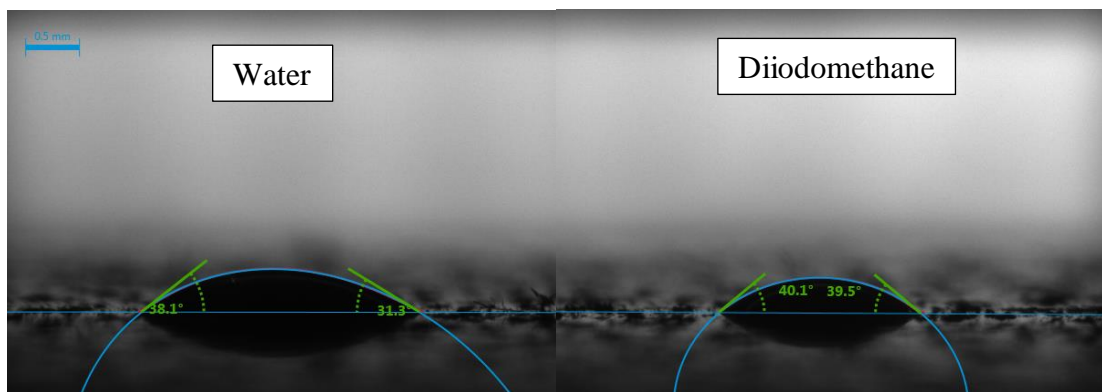


Figure 18: Plasma treated CF/PPS surface

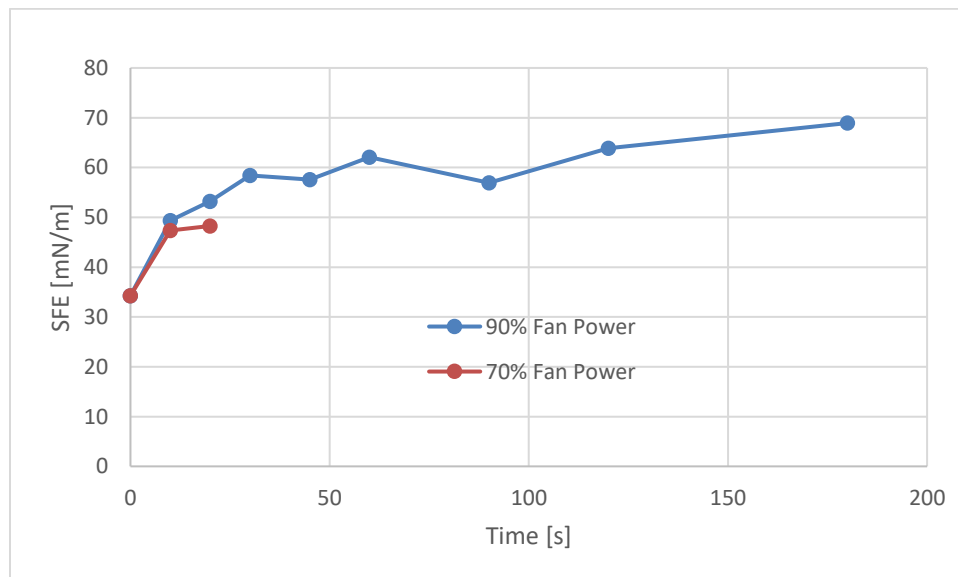


Figure 19: Effect of plasma treatment time on surface free energy

As seen in Figure 19 similar maximum surface free energy results were obtained to the surface free energy found in literature. Therefore, all specimens tested for the two adhesives were given a plasma treatment of 180 second at a fan speed of 90% and a head height of 10 mm.

3.3.2 Adhesive Joint Preparation

After the surfaces were activated using the plasma treater the test specimens could be assembled. For Adhesive 1 the two parts of the adhesive were combined in a small bowl and applied to the surfaces. The area of application was 25 mm x 25 mm, and the two halves were joined together to form a lap shear joint. Paper spacers were inserted onto the specimen supports to attempt to maintain a consistent bond line of 4-6 mils.

Specimens were cured using the manufacturers recommended parameters. Specimens were set out over night at room temperature, then in the morning were treated at 65.5 °C for an hour in an oven. Throughout the curing process the specimens were kept under a constant pressure of about 30 psi using large steel plates set upon them. An example of a specimen's bond line is seen in Figure 20.

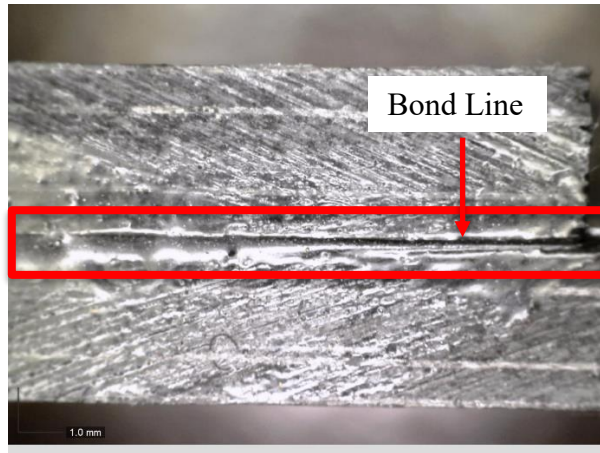


Figure 20: Adhesive 1 bond line

Specimens prepared using Adhesive 2 had a far easier application process. A 25 mm x 25 mm square of the film adhesive was cut, then sandwiched between the two composite halves. A 25 mm spring clamp was then applied to the bond area to maintain pressure as they were cured. The curing process involved a 90 minute cure in a 107 °C oven.

After curing the specimen bond areas were recorded. Testing was done on the same Instron 100 kN servo hydraulic frame used in the bearing testing. Specimens were loaded a rate of 13 mm/min as outlined in ASTM D5868. Load and cross head displacement were recorded at a rate of 5 Hz through the Instron console.

3.3.3 Adhesive Results

Damage observed on specimens treated with Adhesive 1 showed primarily adhesive damage, compared to the preferable cohesive damage. Specimens showed minimal fiber pull out and instead appeared to fail at the surface. As seen in Figure 21 there are large failure lines circled in red. Additionally, the glossy adhesive is clearly seen on both specimens.

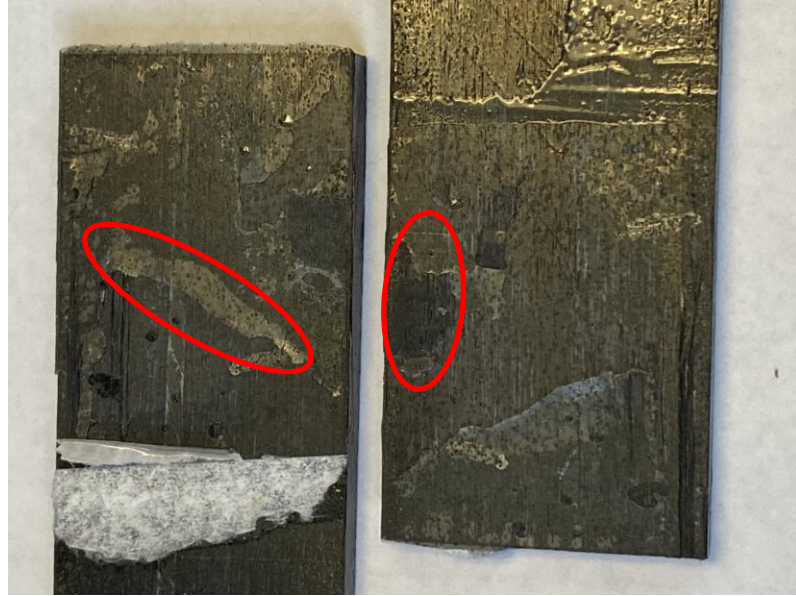


Figure 21: Failed Adhesive 1 Specimen

Adhesive 2 shows a very different failure mode. As seen in Figure 22, the specimen has bonded well with the specimen and in turn has resulted in fiber pull out. This is a much preferred failure mode as it shows failure of the matrix, instead of failure of the adhesive. Additionally, little adhesive is seen on the specimens after failure, only a small portion of the purple film is seen on the upper edge of the part.



Figure 22: Failed Adhesive 2 Specimen

The strength of the joint is calculated via Equation 5.

$$F^{adh} = \frac{P^{max}}{w \times h}$$

Equation 5

Where:

F^{adh} = ultimate bearing strength, MPa [psi]

w = bond area width, mm [in]

h = bond area height, mm [in]

P^{max} = maximum force prior to failure, N [lbf]

The strength of Adhesive 1 was found to be 5.23 MPa, and Adhesive 2 was found to be 18.3 MPa. While Adhesive 2 is clearly the preferred adhesive due to its higher strength and ease of use, both adhesive still provide relatively low strength when compared to the bearing results. Therefore, it was determined that bolted joints would be the primary focus of the research going forward and that there would not be much benefit of exploring a hybrid adhesive-bolted joint.

3.4 Additional Properties

As part of additional work completed for another task on this project material properties were determined experimentally for the CF/PPS from Manufacturer B. A summary of those properties, as well as their associated test standards is given in Table 6 for unidirectional specimens and Table 7 for quasi-isotropic specimens. At the time of the writing of this thesis the only testing that is complete is shear, flexure and short beam strength.

Table 6: Experimentally determined properties for unidirectional specimens

Test	ASTM #	Modulus [GPa] (%COV)	Strength [MPa] (%COV)
Flexure	D6272	112 (3.3)	1180 (9.6)
Shear*	D7078	2.68 (2.4)	-
Short Beam Strength	D2344	-	36 (9.5)

* Note, shear testing used a cross ply [0/90] stacking sequence

Table 7: Experimentally determined properties for quasi-isotropic specimens

Test	ASTM #	Modulus [GPa] (%COV)	Strength [MPa] (%COV)
Flexure	D6272	52.4 (1.1)	461 (9.8)
Shear	D7078	15.3 (5.0)	-
Short Beam Strength	D2344	-	-

3.5 Conclusions

Material characterization tests were completed to better understand the interaction of carbon fiber reinforced polyphenylene sulfide in joining methods. The two joining methods investigated during this study were bolted and adhesive connections. A literature review was presented for each method. Bearing testing was conducted to determine bolted connection strengths and responses for CF/PPS materials from two different manufacturers. It was found that the materials behaved similarly in terms of strength, but the material from Manufacturer B was preferred due to its more linear elasticity curve.

Adhesive joint testing consisted of testing two different adhesives. A plasma treatment device was used to increase the surface free energy of the composite surfaces. Optimal parameters for the device were determined. A comparison of the adhesives then followed and Adhesive 2 was determined as the preferred adhesive. However, adhesive testing yielded strengths much less than that of bolted connections. Therefore, it was determined that bolted connection would be the focus of the research going forward.

Lastly, experimentally determined properties of the CF/PPS from Manufacturer B was presented.

CHAPTER 4: COMPOSITE BEAM JOINT PROTOTYPE

This chapter outlines the design, manufacturing, and testing of a small scale structural prototype. First, the design concept is presented, including load classifications and support conditions. Second, a design process is explained that includes estimating deflections using Timoshenko beam theory, classic laminate theory (CLT), and finite element modeling and analysis (FEM/FEA). Third, prototype construction and testing is documented. Lastly, results of the prototype testing are reported and discussed.

4.1 Introduction

As part of this research an objective was to assess the feasibility of replacing an existing metallic structure with a thermoplastic composite. Previous chapters have outlined the processing and characterization work completed to help guide the design of a structural joint. In this chapter the work is centralized around verifying that a composite replacement is a valid design concept, and then testing a physical small scale prototype to confirm that design.

To be able to understand the stiffnesses and strengths that the composite structure must endure a logical first step is examining the materials used in the current structure.

Currently, the two support decks are made from four aluminum I-beams. Properties of the aluminums used in the structure are summarized in Table 8.

Table 8: Properties of existing aluminum members

Location	Material	Elastic Modulus [GPa]	S_{ut} [MPa]	S_y [MPa]
Web and Top Flange	2014-T6	72.4	483	414
Bottom Flange	7050-T76511	71.7	544	386

Due to the high stiffnesses and strengths it was determined that CF/PPS would be the material of choice for this project as it outperforms many of the glass based composites discussed earlier.

4.1.1 Load Definition

Two separate loading conditions were specified for this project. Load Case 1 features a mass of 109 tonnes distributed over a length of 6.1 m. Load Case 2 features a lower mass of 77 tonnes distributed over a length of 4.6 m. Both load cases are subject to an impact factor of 1.2 applied to the loading condition's mass. Additionally, there are other loads that are applied to the structure such as a dead load of 13.6 tonnes and a load of 4.8 tonnes distributed evenly along the length of the structure.

Support conditions for this structure include a contact length of 0.75 m. The structure is free to rotate about this point on either side.

To determine the limiting load case bending moment and shear force calculations were conducted. It was determined that Load Case 1 yielded the greatest bending and shear forces over Load Case 2. Using a center positioned load, Load Case 1 resulted in a

maximum bending moment of 1251.5 kN·m and a maximum shear force of 180.9 kN.

Load Case 2 had a maximum bending moment of 1013 kN·m and a maximum shear force of 135.1 kN. Additionally, critical loading scenarios such as the rear edge of the load being centered to the structure were examined. This resulted in an increase in shear force at the center of the structure and a decrease of the bending moment. It was determined that Load Case 1 was the limiting load and that maximum bending occurred at the center of the structure when the mass was centrally located, and that the maximum shear force occurred when the rear edge of the mass was in line with the center.

The final loading data that was provided was the midpoint deflections of the current structure under a multitude of loading conditions. These provided a reference point for acceptable deflections of the composite structure under loading. The load and deflections are summarized in Table 9.

Table 9: Acceptable beam deflections

Load Type	Deflection [in]	Deflection [m]
Working Load	11.825	0.30035
Overload	16.455	0.41796
Ultimate Load	18.626	0.47310

4.2 Laminate Analysis

One of the valuable tools needed to design and analyze composite laminates is classical laminated plate theory (CLPT). This powerful tool helps relate lamina properties of the composite tapes to effective properties found in the final laminate. A matlab script was written to calculate these effective moduli for use in other scripts developed for this project. This section will serve to explain the theory and logic behind the code. The code was developed as part of MEE 550: Mechanics of Laminated Composite Structures.

First, it is important to specify the properties that the user will input. Lamina properties are required including: longitudinal and transverse Young's modulus (E_1 and E_2), the in-plane shear modulus (G_{12}), the in plane Poisson's ratio (ν_{12}), and the material thickness (h). The stacking sequence and orientation of the fibers must also be specified. Using these properties effective moduli can be determined.

It is assumed that the laminate is in a state of plane stress. Under this assumption a reduced stiffness matrix (Q) for each lamina can be constructed with Equation 7. To determine the reduced stiffness matrix the minor poisons ratio (ν_{12}) must be calculated per Equation 6.

$$\nu_{21} = \nu_{12} \frac{E_2}{E_1}$$

Equation 6

$$[Q] = \begin{bmatrix} Q_{11} & Q_{12} & Q_{16} \\ Q_{12} & Q_{22} & Q_{26} \\ Q_{16} & Q_{26} & Q_{66} \end{bmatrix} = \begin{bmatrix} \frac{E_1}{1 - \nu_{12}\nu_{21}} & \frac{\nu_{12}E_2}{1 - \nu_{12}\nu_{21}} & 0 \\ \frac{\nu_{12}E_2}{1 - \nu_{12}\nu_{21}} & \frac{E_2}{1 - \nu_{12}\nu_{21}} & 0 \\ 0 & 0 & G_{12} \end{bmatrix} \quad \text{Equation 7}$$

Once the reduced stiffness matrix is calculated it must be transformed from its local lamina coordinate system into the global laminate coordinates. This is calculated for each layer using the off-axis reduced stiffness matrix. Equation 8 thru Equation 14 outline the process. The lamina orientation angle (θ) is used to relate the lamina to the global coordinate system. Constant m and n are determined for each layer, where $m = \cos(\theta)$ and $n = \sin(\theta)$.

$$[\bar{Q}] = \begin{bmatrix} \bar{Q}_{11} & \bar{Q}_{12} & \bar{Q}_{16} \\ \bar{Q}_{12} & \bar{Q}_{22} & \bar{Q}_{26} \\ \bar{Q}_{16} & \bar{Q}_{26} & \bar{Q}_{66} \end{bmatrix} \quad \text{Equation 8}$$

$$\bar{Q}_{11} = Q_{11}m^4 + 2(Q_{12} + 2Q_{66})m^2n^2 + Q_{22}n^4 \quad \text{Equation 9}$$

$$\bar{Q}_{12} = (Q_{11} + Q_{22} - 4Q_{66})n^2m^2 + Q_{12}(n^4 + m^4) \quad \text{Equation 10}$$

$$\bar{Q}_{16} = (Q_{11} - Q_{12} - 2Q_{66})nm^3 + (Q_{12} - Q_{22} + 2Q_{66})n^3m \quad \text{Equation 11}$$

$$\bar{Q}_{22} = Q_{11}n^4 + 2(Q_{12} + 2Q_{66})n^2m^2 + Q_{22}m^4 \quad \text{Equation 12}$$

$$\bar{Q}_{26} = (Q_{11} - Q_{12} - 2Q_{66})n^3m + (Q_{12} - Q_{22} + 2Q_{66})m^3n \quad \text{Equation 13}$$

$$\bar{Q}_{66} = (Q_{11} + Q_{22} - 2Q_{12} - 2Q_{66})n^2m^2 + Q_{66}(n^4 + m^4) \quad \text{Equation 14}$$

Next, the laminate stiffness matrices [A], [B], and [D] can be calculated. This is done using a through thickness integration technique. As each layer is piecewise constant a numerical summation is utilized as outlined in Equation 15 thru Equation 17. The z value refers to the through thickness coordinate, where $z_1 = 0$ and $z_{N+1} = h^*$ (number of layers).

$$[A] = \sum_{k=1}^N (z_{k+1} - z_k) [\bar{Q}]^{(k)} \quad \text{Equation 15}$$

$$[B] = \frac{1}{2} \sum_{k=1}^N (z_{k+1}^2 - z_k^2) [\bar{Q}]^{(k)} \quad \text{Equation 16}$$

$$[D] = \frac{1}{3} \sum_{k=1}^N (z_{k+1}^3 - z_k^3) [\bar{Q}]^{(k)} \quad \text{Equation 17}$$

The laminate stiffness matrices can be combined to form the [ABD] matrix by Equation 18. Additionally the [ABD] matrix can be inverted to determine the laminate compliances. This is known as the [abd] matrix and is derived by Equation 19.

$$[ABD] = \begin{bmatrix} [A] & [B] \\ [B] & [D] \end{bmatrix} \quad \text{Equation 18}$$

$$[abd] = [ABD]^{-1} = \begin{bmatrix} [a] & [b] \\ [b^T] & [d] \end{bmatrix} \quad \text{Equation 19}$$

Effective laminate properties can then be determined using Equation 20 thru Equation 23 where H refers to the laminate thickness.

$$\bar{E}_x = \frac{1}{a_{11}H} \quad \text{Equation 20}$$

$$\bar{E}_y = \frac{1}{a_{22}H} \quad \text{Equation 21}$$

$$\bar{\nu}_{xy} = \frac{-a_{12}}{a_{11}} \quad \text{Equation 22}$$

$$\bar{G}_{xy} = \frac{1}{a_{33}H} \quad \text{Equation 23}$$

These properties can be used in calculations as a simple approximation of expected laminate response.

4.2.1 Timoshenko Beam Assumption

A matlab script was developed to allow for rapid analysis of a variety of structural and laminate designs. Finite element models are often complex and require considerable computational power. To simplify initial design analysis, Timoshenko beam assumptions were used to calculate the mid-span deflection. This mid-span deflection could then be used to compare the design to known deflection as prescribed in Table 9. Upon finding a promising design the analysis would then be conducted using FEA in Abaqus.

The critical loading scenario occurs when the large mass is centrally loaded on the structure. Timoshenko beam theory is most useful with either a point load or a load distributed across the entire structure evenly. Therefore, it was decided that this script would act more to bound the problem than to provide an exact deflection. A point load would overestimate the deflection, whereas an evenly distributed load would underestimate. The actual response of the structure is expected to fall somewhere in between these two assumptions.

Using an even distribution of the mass across the structure a central maximum deflection could be calculated with Equation 24. Whereas, a consolidated point load would yield a maximum central deflection calculated by Equation 25.

$$\delta_{\max}^D = \frac{5}{384} \frac{qL^4}{EI} + \frac{1}{8} \frac{qL^2}{GA_c} \quad \text{Equation 24}$$

$$\delta_{\max}^P = \frac{1}{48} \frac{PL^3}{EI} + \frac{1}{4} \frac{PL}{GA_c} \quad \text{Equation 25}$$

Where:

q = distributed load, kN/m [lbs/in]

L = length of the span, m [in]

E = Young's modulus, MPa [psi]

I = second moment of area of the cross section, m⁴ [in⁴]

G = Shear modulus, MPa [psi]

A_c = cross sectional area, m² [in²]

P = point load, kN [lbs]

Using these governing equations a script could be developed. Three beam shapes were selected for this research: an I-beam, a rectangular box beam, and a double web I-beam. The user is able to specify which one of these shapes they would like to perform an analysis with. The user is then able to specify the desired lamina properties (E_1 , E_2 , ν_{12} , G_{12} , h) to use for the analysis, as well as the composite laminate stacking sequences. The code allows for different laminates to be used in the upper flange, lower flange, and web. The user is then asked to specify cross sectional area properties such as flange widths and web height. Finally, the user can input load factors such as mass properties, impact factors, and additional loading criteria. Once all factors are specified the code can run.

First, the code calculates the effective moduli using classical laminate plate theory as outlined in the previous section. Then, depending on beam type selected, the code determines the location of the centroid (Equation 26) and the second area moment of inertia (Equation 27) with respect to the y-axis. Y-axis refers to the vertical dimension of the beam cross section. As each beam type can be discretized into a series of rectangles the equations are written to perform piecesise calculations.

$$\bar{y} = \frac{\sum A_i y_i}{\sum A_i} \quad \text{Equation 26}$$

Where:

A_i = cross sectional area of each beam component, m² [in²]

y_i = coordinate of each segment's center as measure from the bottom of the beam, m [in]

$$I_{yy_i} = \frac{b_i h_i^3}{12} + A_i (y_i - \bar{y})^2 \quad \text{Equation 27}$$

Where:

b_i = horizontal measurement of each beam component, m [in]

h_i = vertical measurement of each beam component, m [in]

N = number of discretized beam elements

The code then determines the total stiffness of the beam (EI) by summing the stiffnesses of each section (Equation 28). The E_x value obtained from the CLPT code for each section is used as the modulus.

$$I_{yy} = \sum_{i=1}^N E_{x_i} I_{yy_i} \quad \text{Equation 28}$$

The shear area (A_c) and modulus (G_{xy}) is assumed to be that of the web as that is the expected path the load will take. As all loads, rigidities, and geometries have been

defined the code is then able to calculate the deflections with Equation 24 and Equation 25. The complete code can be found in APPENDIX B.

4.3 Design Theory

Utilizing the code developed in the prior sections many different cross sections and beam sizes were examined. It quickly became clear that a box or double web I-beam cross section would be preferable due to their increased stability compared to an I-beam. At this stage a focus was put on the manufacturability of the composite structure. Based on findings in research [45] a modular composite construction technique would be used. Large flat plates of fiber reinforced thermoplastic composites can be consolidated then joined together through metallic connectors. The initial design pursued was a T-style aluminum connector. Aluminum was selected as it is lightweight and can be extruded to make the profile. The connector, seen in Figure 23, allows for three composite plates to meet at a point. Using 4 connectors and 8 composite plates a double web I-beam can be constructed. Bolts/rivets can be inserted through the aluminum and composite panels to join them together along the length of the connector.

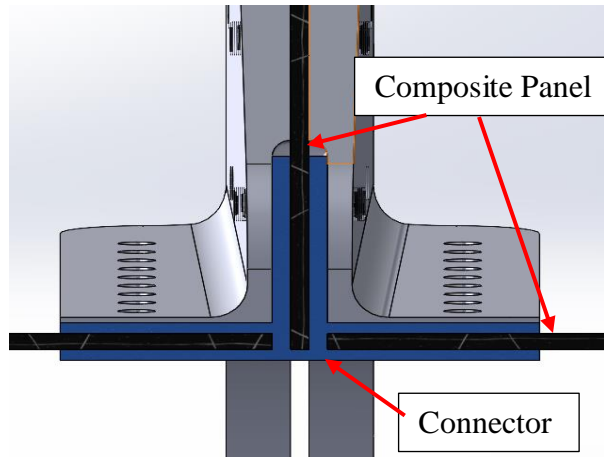


Figure 23: T-style aluminum connector

While possible, cost and fabrication time was determined to be too great for this style connector. A redesign was done to instead use two pieces of 90 degree aluminum stock and a piece of flat plate. This would drastically cut down on cost and manufacturing time as these aluminum pieces are readily available from many retailers. Additionally, the redesign allowed for a continuous bottom composite plate to be used which helps stiffen the structure. The redesigned connector is seen in Figure 24. Aluminum wall thicknesses of 9.5 mm were selected to match the thickness of the composite plates.

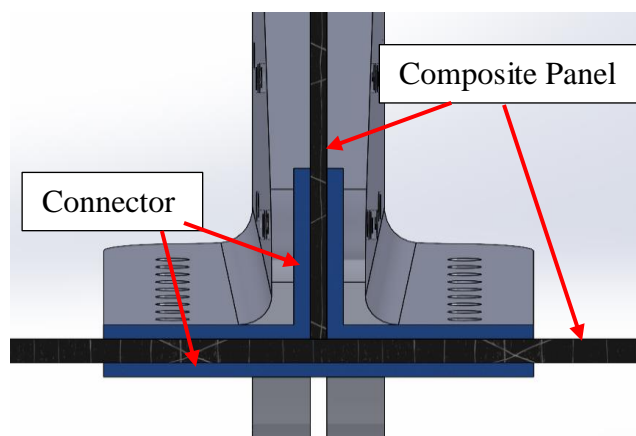


Figure 24: L-style aluminum connector

Design considerations were also made for the geometry of the beam. It was determined that the most logical design would be one that occupied the same footprint as the existing metallic structure. The existing structure uses four I-beams to create two load decks. To provide increased stability and strength it was determined that it would be more advantageous to use two double web I-beams to support the two decks. It was also determined that the composite plates used to construct the beam section should be the same thicknesses as the existing aluminum parts. The webs and upper flange of the structure are 9.5 mm thick, and the bottom flange is 15.9 mm thick. These decisions created the dimensions that could then be analyzed more thoroughly using finite element analysis.

4.4 FEA Modeling

A finite element model was to predict deflections and examine failure of the composite structure. This was done for both the full scale bridge, as well as the prototype. Tsai-Wu failure criterion was used to assess failure of the composite panels. This through thickness approach predicts failure if the stresses in each lamina exceed a failure index, I_f of 1, specified by Equation 29.

$$I_f = f_1\sigma_1 + f_2\sigma_2 + f_{11}\sigma_1^2 + f_{22}\sigma_2^2 + f_{66}\tau_{12}^2 - \sqrt{f_{11}f_{22}}\sigma_1\sigma_2 \quad \text{Equation 29}$$

Where:

σ_1 = axial stress in the 1-direction, MPa [psi]

σ_2 = axial stress in the 2-direction, MPa [psi]

τ_{12} = Shear stress in the 1-2 plane, MPa [psi]

The Tsai-Wu failure coefficients are given as Equation 30 thru Equation 34.

$$f_1 = \frac{1}{F_{1t}} - \frac{1}{F_{1c}} \quad \text{Equation 30}$$

$$f_{11} = \frac{1}{F_{1t}F_{1c}} \quad \text{Equation 31}$$

$$f_2 = \frac{1}{F_{2t}} - \frac{1}{F_{2c}} \quad \text{Equation 32}$$

$$f_{22} = \frac{1}{F_{2t}F_{2c}} \quad \text{Equation 33}$$

$$f_{66} = \frac{1}{F_6^2} \quad \text{Equation 34}$$

Where:

F_{1t} = Longitudinal tensile strength, MPa [psi]

F_{1c} = Longitudinal compressive strength, MPa [psi]

F_{2t} = Transverse tensile strength, MPa [psi]

F_{2c} = Transverse compressive strength, MPa [psi]

F_6 = In-plane shear strength of the lamina in the principal coordinate system, MPa [psi]

The strengths used in Equation 30-Equation 34 are from the manufacturer and are summarized in

Table 10.

Table 10: Strength properties of CF/PPS

Property	[MPa]
F_{1t}	1972
F_{1c}	897
F_{2t}	22.7
F_{2c}	101
F_6	43.1

Abaqus was selected as the finite element analysis program due to its power and ready availability. The modeling process will now be discussed for each model type.

4.4.1 Full Scale Model

The full scale finite element model was refined through multiple revision that increased in complexity. The first model used was a beam that contained no hardware and was developed to model simple responses of the structure to load. The model used a constant extruded shell cross section that was the same size as the existing metallic structure. The model consisted of two parts, joined at the center with four constrained points. These points represented where the aluminum hinges would join the structure together and were restrained in u_1 , u_2 , and u_3 degrees of freedom to each other. This model is seen in Figure 25.

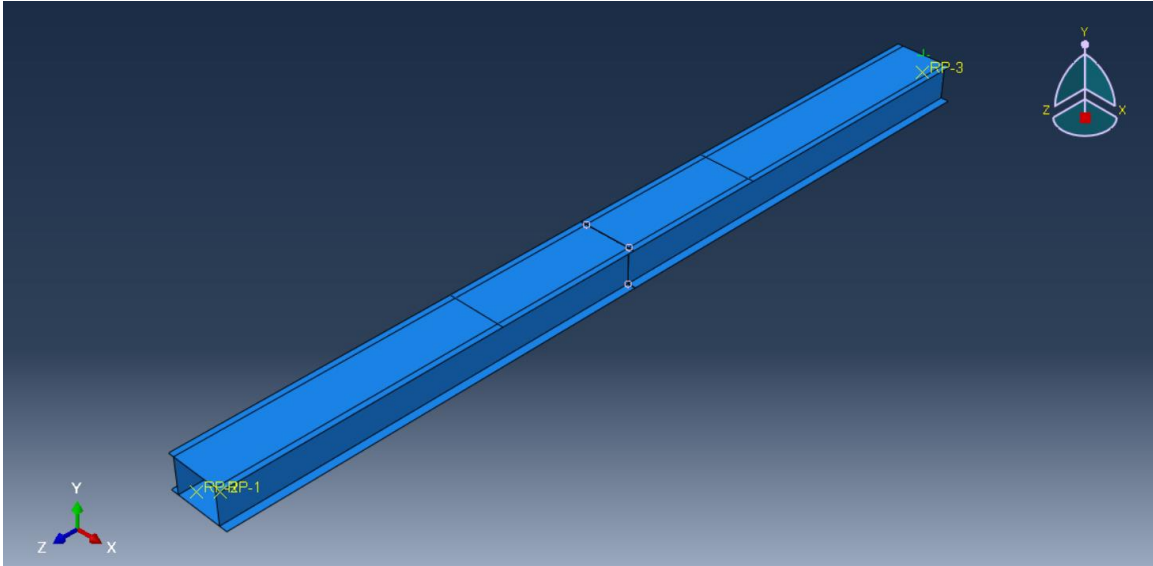


Figure 25: Simple FEA full scale beam

Beam sections were given composite layups using abaqus's composite layup tool.

Material properties were specified using the technical data sheet from Manufacturer B.

Layups were defined as outlined in Table 11 for each section of the beam. The 0 degree direction of the fiber was aligned with the global z-axis. These layups were designed to provide additional axial strength through the inclusion of proportionally more 0 degree layers in the flanges, and to provide a more quasi isotropic response in the web through the use of a (0/±45/90) stacking sequence.

Table 11: Composite layup for FEA model

Location	Layers (Thickness)	Layup	Ex (GPa)	Gxy (GPa)	% 0° Fiber
Upper Flange	68 (9.5 mm)	[0 ₂ /(0 ₂ /±45/90) ₅ /0 ₇] _s	72.50	11.07	55%
Web	68 (9.5 mm)	[(0/±45/90) ₈ /0/90] _s	44.76	15.65	26%
Lower Flange	114 (16 mm)	[0/(0 ₃ /±45/90) ₈ /0 ₈] _s	74.39	10.72	58%

Loads were applied to the structure evenly through a series of pressures. A load of 4250 kN/m² was applied to the far regions of the structure and a load of 98,000 kN/m² was applied to the center region. Boundary conditions were modeled as a roller-pin support where the left edge was pinned and the right edge was on a roller. Boundary conditions and loads are seen in Figure 26.

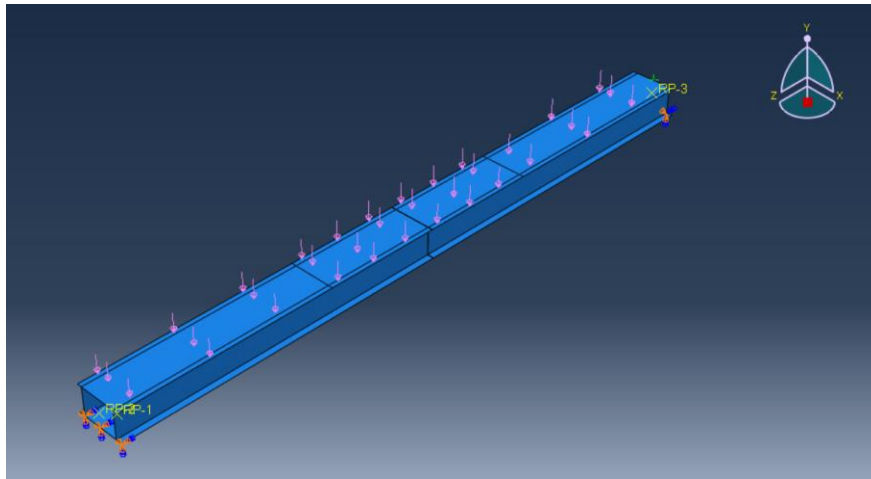


Figure 26: Full FEA beam loading

The model was meshed with S8R elements. These shell elements are of quadratic order and have 6 degrees of freedom per node. Convergence was obtained with a total of 7004 elements used, connected by 21,164 nodes. This structure was primarily examined for mid-span deflection, which was found to be 0.273 m (Figure 27).

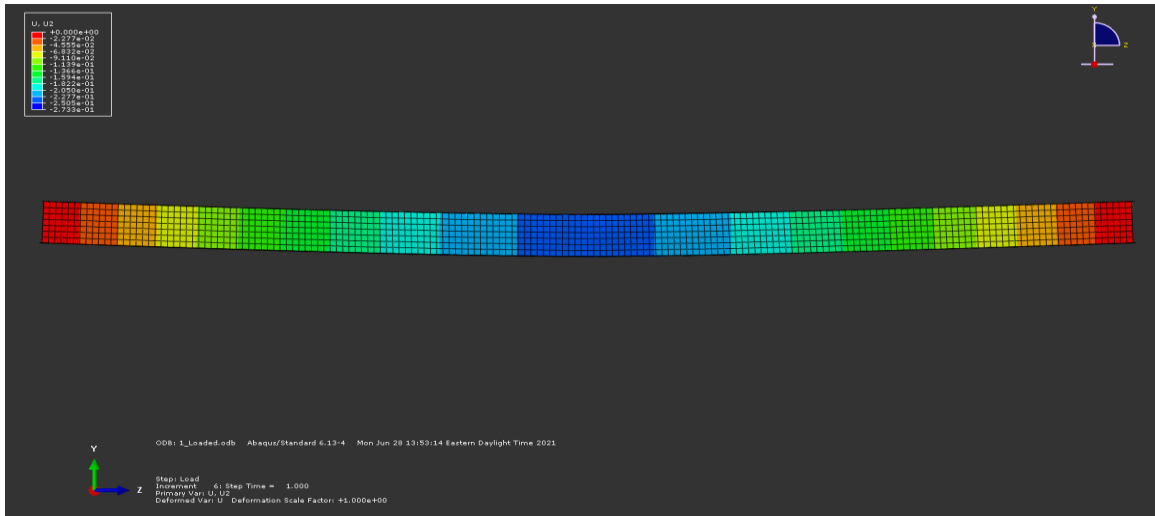


Figure 27: Deflections of simple FEA full beam

This mid-span deflection was of a similar magnitude as those experimentally observed by the project sponsor with a metallic structure; therefore, this design concept was determined to be function and could move forward with further development. The next model developed was one that incorporated the hinges used in the structure. This model would also take advantage of the bridge having symmetry along its length. Therefore, this model became known colloquially as the $\frac{1}{2}$ full length model. This model, seen in Figure 28, utilized the same dimensions discussed in the previous section, but incorporated simplified versions of the upper and lower hinges with pins inserted for restraint.

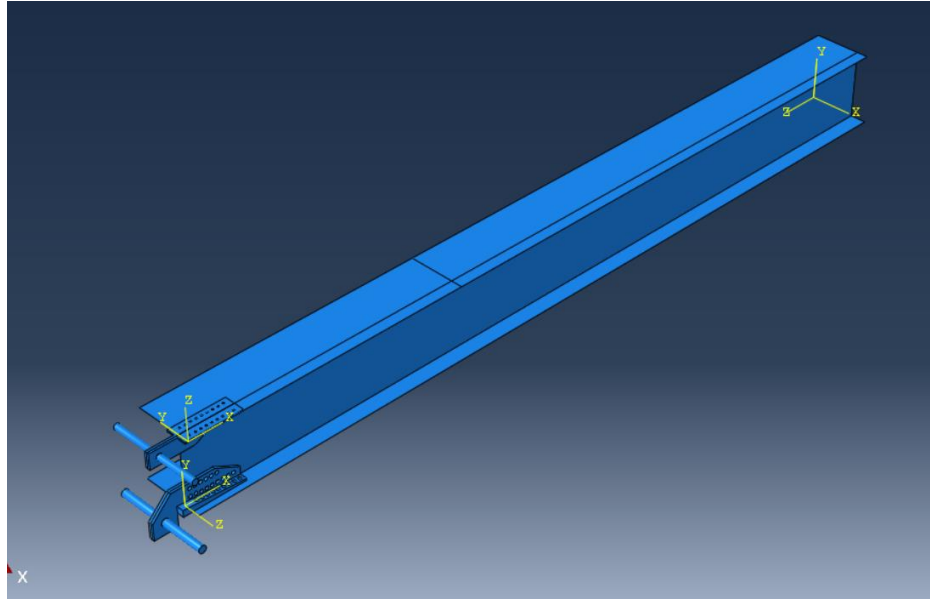


Figure 28: $\frac{1}{2}$ full length FEA model

Laminates were defined using the same stacking sequence outlined in Table 11. The hinges were defined using properties of their prescribed aluminum alloy. Shell to solid coupling constraints were used to connect the bolt holes on the laminate to the hinges. These allow for the transfer of nodal displacements along a shell edge to a set of nodes on a solid surface. Additionally surface to surface hard contact interactions were defined between the hinges and pins to support the left edge of the structure.

Loading was defined using the same pressures outlined in the previous model. To simulate the joining at the hinge the pins were restrained in all degrees of freedom except vertical displacement (u_y). The rear edge was supported as a pinned connection. To simulate the symmetry about the center of the beam, one displacement (u_x) and two rotations (R_y, R_z) were constrained. S8R quadratic shell elements were used to model the composite shells and C3D310 quadratic order solid tetrahedral elements were used to model the hinge and pins.

The structure was analyzed and failure criteria were examined. Displacements were observed to be 0.186 m in the vertical direction. The full displacement field is shown in Figure 29.

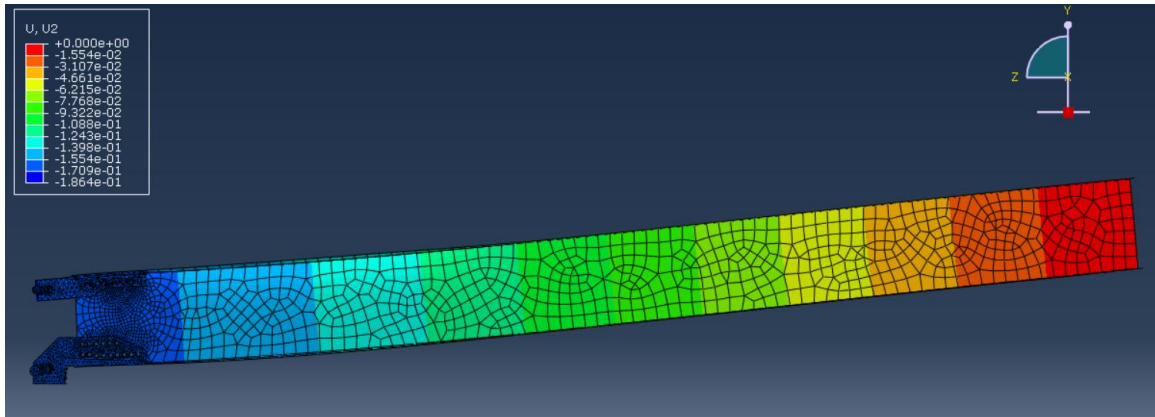


Figure 29: Displacement field of 1/2 full bridge structure

Areas of interest were examined for failure. These include interlaminar stresses in the webs as well as stress concentrations around bolt hole. Through-thickness tsai-wu failure was examined at these points of interest. Maximum failure indices were observed on exterior surfaces near the bolt holes; however, all were well below the failure index of 1 and predict that the structure will not fail. An example through-thickness graph is shown in Figure 30. Note that on this graph Abaqus outputs the scaling factor R , which is the reciprocal of the safety factor, S_f . Values $R < 1.0$ indicate that the state of stress is within the failure surface, while values $R \geq 1.0$ indicate failure.

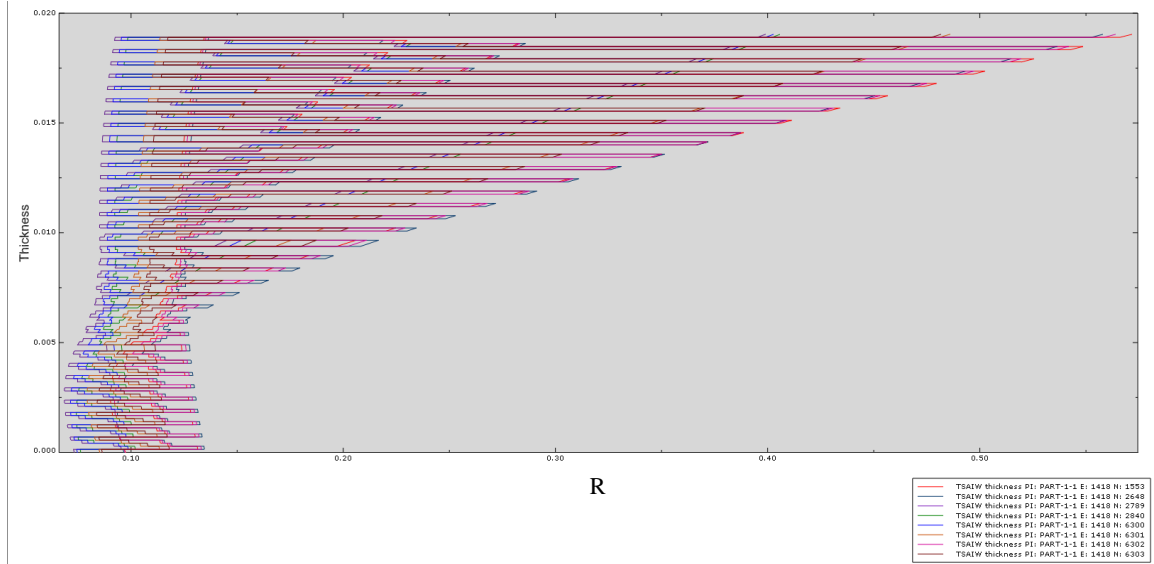


Figure 30: Through thickness scaling factor graph

Additionally, von mises stresses were examined around the bolt holes. Stress concentrations ranged from approximately 100 – 400 MPa (Figure 31), which was well below the ultimate bearing strength of approximately 550 MPa. Therefore, failure due to bearing forces around the bolts is not expected.

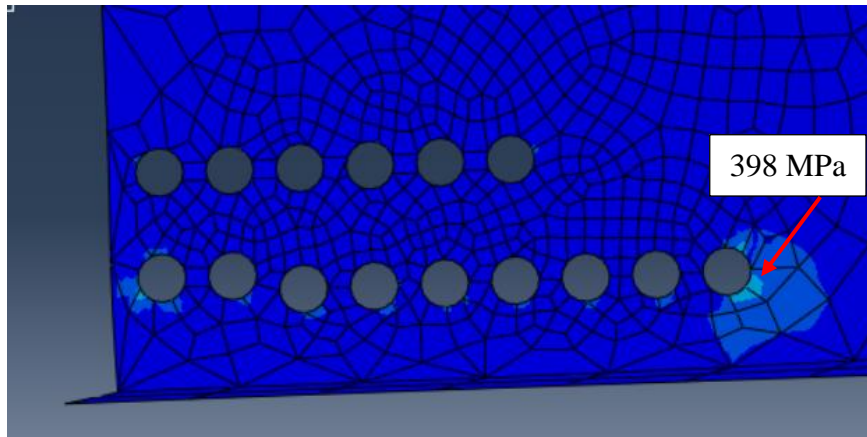


Figure 31: Stress concentration at bolts

The next step for the full scale model was to incorporate all bolts and bolt holes needed for the final structure. This became too computationally intensive for the full scale model

as over 400 fasteners would have to be modeled, even with a decreased size due to symmetry. Therefore, it was decided that a prototype scale model would be pursued that incorporated all fasteners and would be able to be compared to laboratory mechanical testing.

4.4.2 Prototype Scale Model

An additional FEA model was created to analyze the response of the prototype section. The prototype was designed to have the same cross section as the full scale model, but only be 1.016 m in length due to size limitations of the hydraulic press used to manufacture the composite panels. This model would also only feature the bottom hinge as that was the only hinge received by UMaine for testing. Boundary conditions were also updated to accurately capture the physical test setup.

The structure, shown in Figure 32, was constructed in a similar manner as the full scale prototype. The web and flanges were modeled as shells and the hinges, bolts, aluminum sections and pins were modeled as 3D solid elements. All items were assembled with contact pairs between surfaces that may intersect during loading. Similar to the full scale model, the composite bolt holes were mated to the solid bolts using shell to solid coupling. The prototype loading was evenly distributed across the surface of the top flange using a pressure load. Pin boundary conditions were applied to the rear edge of the structure and the front pin was constrained in all displacement and rotations except horizontal displacement. These boundary conditions are what the physical prototype will experience in the test frame.

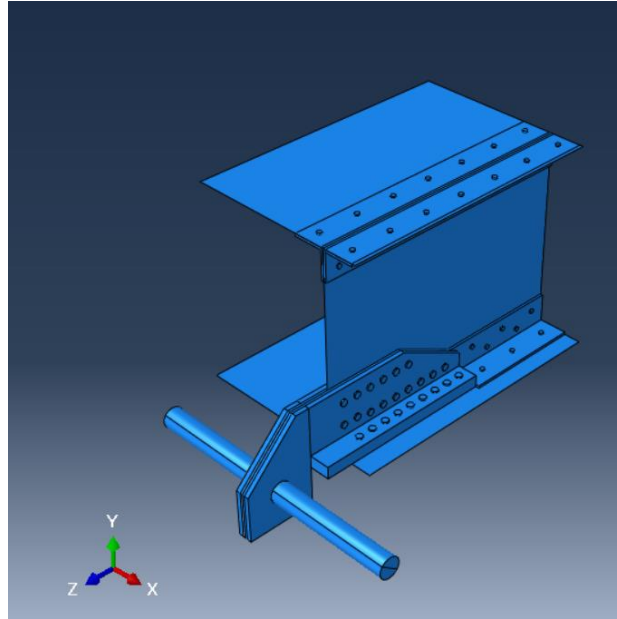


Figure 32: Prototype FEA model

All shell elements were meshed with S8R elements and all solid elements were meshed with C3D20R quadratic order hex elements. These elements provide 20 nodes per element and are considered a quadratic brick element. A total of 691,920 nodes were used to connect 301,394 elements. The model was run and analyzed. A small load of 30 kN spread evenly across the prototype yielded low stresses in the structure. Therefore, failure using tsai-wu or bearing stress was not detected. The other metric of interest was the mid-span deflection of the bottom flange. This was found to be 0.85 mm. The full deflection field is shown in Figure 33. This value is important as it will be used to compare the FEA model response to the physical prototype tested.

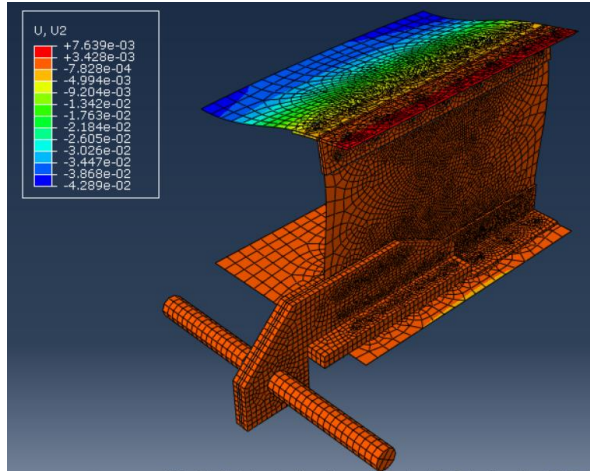


Figure 33: Prototype FEA displacement

As no concerns were noted from the finite element analysis, plans were prepared to test a prototype section in the lab.

4.5 Prototype Beam Section Manufacturing

This section seeks to outline the manufacturing process of the prototype beam section. The manufacturing process began by having to redesign one of the hinge setups upon receiving a truncated hinge. Once the redesign was complete the composite panels were fabricated, as well as the aluminum sections. All components were assembled and the face subject to DIC was prepared. Detailed information on each of these steps is provided below.

4.5.1 Truncated Hinge

As stated earlier the testing was planned to include two male lower hinges provided by the project sponsor. One hinge was received early in the project to allow for accurate measurements to be taken to aid in computer modeling efforts. The second hinge arrived

a few months in advance of testing. Upon arrival the hinge was inspected and it was found that a truncated hinge had been sent. Figure 34 shows the SolidWorks model of the hinge and approximately how it was shortened. This presented a major issue as the design relies on the stiffness of a complete hinge.

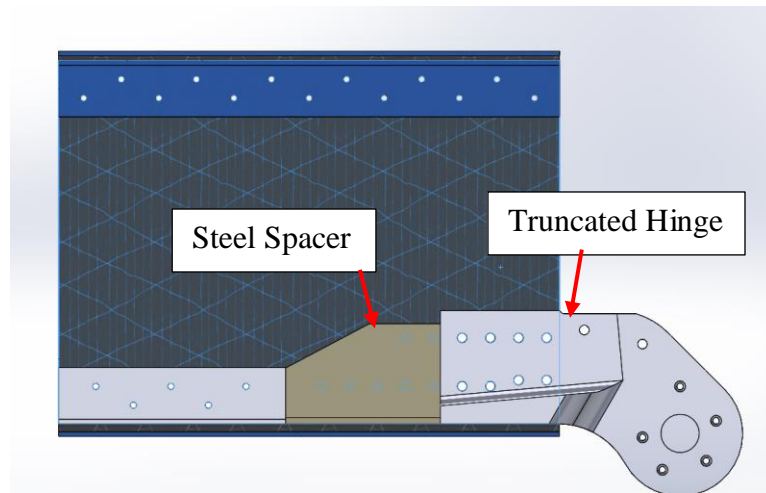


Figure 34: Truncated hinge

After discussion with the sponsor it was determined that the truncated hinge would have to be used. A stipulation was given that any solutions to this problem could not involve physically modifying the truncated hinge. It was determined that material would be added to the rear of the hinge to make up for the missing section. This added material would not be physically attached to the hinge, but rather bolted to the web and bottom flange of the structure. As the web and flange are shared surfaces of the two parts of the modified hinge it was determined that the spacer must maintain similar bending and axial stiffness. Two replacement options were determined, either a steel or aluminum member made from readily available 90 degree angle stock.

To quantify the substitution, the axial and bending stiffness of the existing hinge section, and the two design options were determined. Axial stiffness (k_{axial}) is given by Equation 35 and bending stiffness (k_{bend}) is given by Equation 36.

$$k_{axial} = \frac{EA}{L} \quad \text{Equation 35}$$

$$k_{bend} = \frac{EI}{L^3} \quad \text{Equation 36}$$

Where:

E = Modulus of elasticity, MPa [psi]

A = Cross sectional area, mm² [in²]

I = Area moment of inertia, mm⁴ [in⁴]

L = Section length, mm [in]

In all scenarios the length of the substitute is constant due to geometry constraints; therefore, the results will be reported as EA and EI. The properties of each section are summarized in Table 12. For the aluminum section, a 200 mm x 200 mm x 25.4 mm 90-degree angle was selected made from 6061-T6 aluminum. For the steel section, a 200 mm x 100 mm x 12.6 mm 90-degree angle was selected made from A36 Steel.

Table 12: Hinge replacement decision matrix

Material	EA [kN]	EI [kN·mm ²]
Original Hinge	717,000	3.93e9
Aluminum L	666,000	4.04e9
Steel L	741,800	3.32e9

The aluminum leads to a 7.1% decrease in axial stiffness and an increase of 2.7% in bending stiffness. The steel leads to a 3.4% increase in axial stiffness and a 15.5% decrease in bending stiffness. Given that axial stiffness is a greater factor in the prototype testing it was determined that the steel member would be used. By maintaining relatively similar stiffnesses the structure is expected to have a similar mechanical response to a complete hinge.

The steel member was fabricated at ASCC using a 1.2 m long member of the prescribed steel angle. A combination of horizontal band saw and drill presses were used to create the final part, seen in progress in Figure 35.



Figure 35: Steel replacement for truncated hinge

4.5.2 Panel Fabrication

The prototype composite panels were fabricated using a similar process to the smaller coupon panels outlined earlier in this document. As stated in Chapter 3, the preferred CF/PPS material was supplied by Manufacturer B. However, due to global supply chain

issues caused by COVID-19 the material was unable to be ordered from that manufacturer. Therefore, materials were ordered from Manufacturer A. The CF/PPS tapes were slit to 50 mm widths to minimize waste incurred during the tape layup process. Four blanks were created using the Fiber Forge Tape Layup Machine as summarized in Table 13. The zero degree direction is aligned with the width dimension.

Table 13: Prototype panel dimensions

Panel ID	# of Panels	Length [m]	Width [m]	# of Plies	Orientation
Top_Flange	1	1.394	1.016	46	$[0_2/(\pm 45/90/0_2)_4/0]_S$
Bottom_Flange	1	1.496	1.016	76	$[0_2/(\pm 45/90/0_2)_6/0_6]_S$
Web	2	1.016	0.737	48	$[0/90/\pm 45]_{6S}$

Due to a miscommunication, one of the web panels was laid up incorrectly. Instead of the prescribed stacking sequence a sequence of $[(0/90/\pm 45)_S]_6$ was used. This was corrected in time for the second panel, but was too late to correct for the first panel as it had already been welded. It was determined that the panel could still be used as it would not affect the principal stiffnesses of the panel, but may have a minor impact on out-of-plane properties. To minimize any observed structural effects the panel was assembled on the side opposite the DIC cameras with the truncated hinge.

Once assembled the composite blanks could be consolidated. To maximize panel size it was determined that a mold would not be used for consolidation. Small trials with the CF/PPS showed that there was minimal resin flow during the consolidation process. The 650 metric ton Utah hydraulic press was outfitted with 2 polished aluminum heated

platens to provide the consolidation surface. As with the small panels, the consolidation surfaces were treated with chemlease. Figure 36 shows the consolidation press setup.

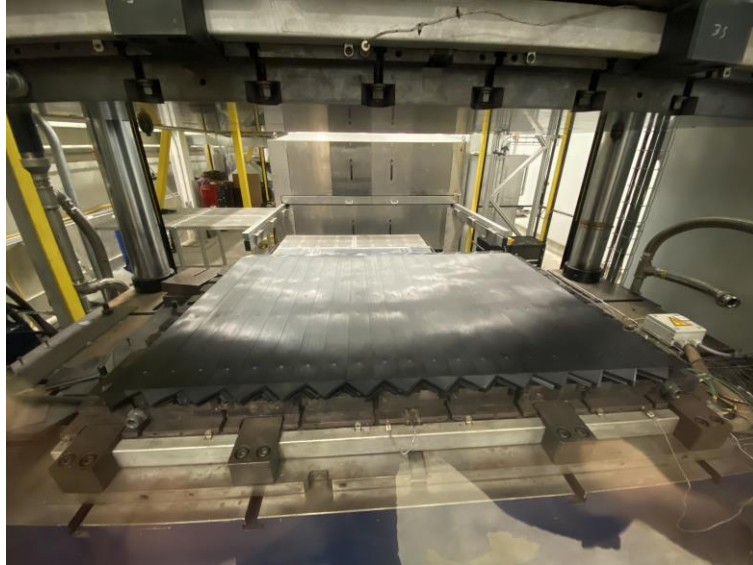


Figure 36: Bottom flange in consolidation press

A similar temperature and pressure cycle as used on the small panels was applied. The set temperature was slightly reduced to prevent excessive resin flow and the dwell time was increased to make sure an even temperature distribution was achieved in the part. The temperature cycle for one of the webs, as recorded by the press, is shown in Figure 37. The press does not feature active cooling so the panels were monitored to make sure they did not cool too fast to inhibit crystallization formation. After the crystallization temperature was achieved the press was allowed to cool overnight. In the morning the hydraulic pressure was released and the part was removed.

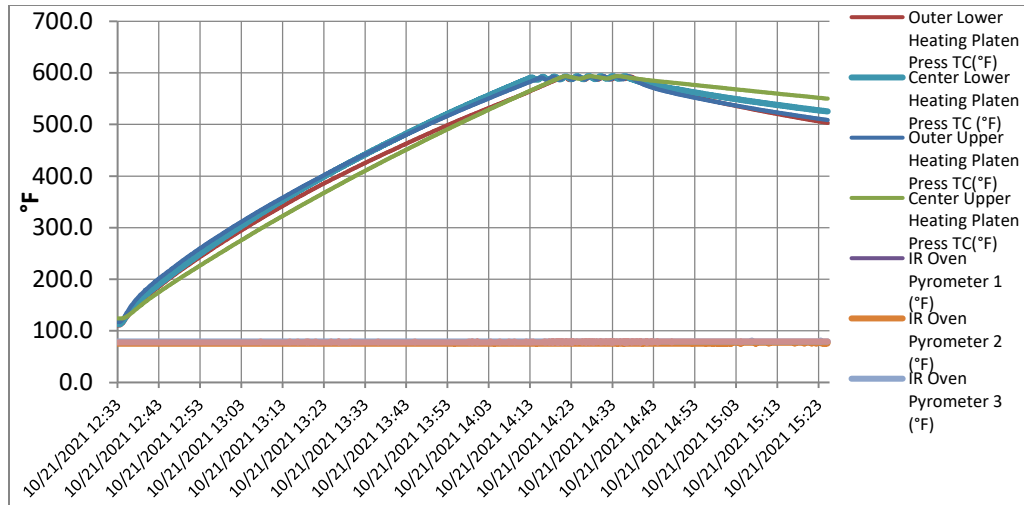


Figure 37: Press temperature cycle

Finished parts were then inspected. Minor surface defects were observed but were minimal. Due to the core consisting of 0 degree fibers there was minor fiber and resin squeeze out on the flange panels, as seen in Figure 38.



Figure 38: Flange fiber squeeze out

Finished panels were then trimmed to final dimension on the water-jet. Bolt holes were water-jet cut into the panels to provide accurate hole placement for assembly. A completed web panel is seen in Figure 39.

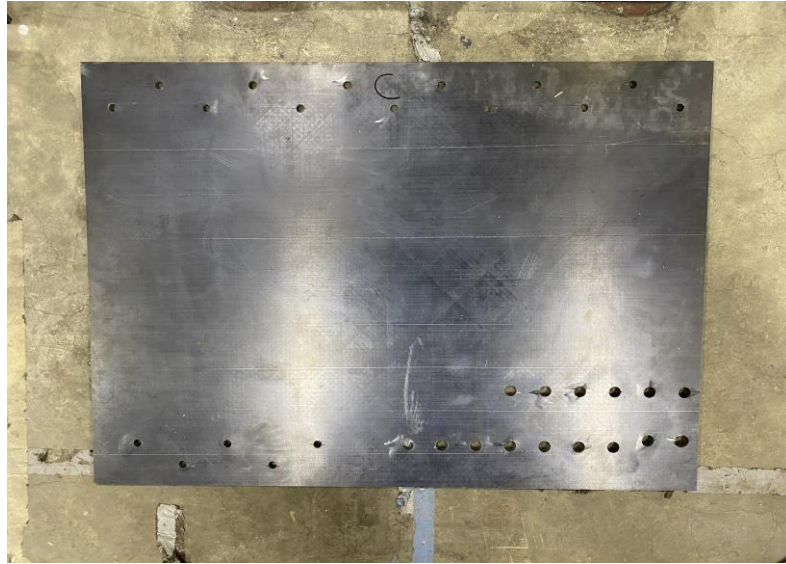


Figure 39: Web panel with bolt holes

4.5.3 Aluminum Section Processing

Aluminum sections were processed using the equipment found at ASCC. Four 2.44 m long pieces of 9.5 mm thick, 150 mm legged, 90 degree angle stock made from 6061 aluminum were utilized, as well as four pieces of 9.5 mm thick 6061 aluminum rectangular plate, measuring 0.3 m by 1.2 m. Using a combination of machining operations on the horizontal band saw, circular saw, drilling machine and bench sander all pieces were processed to their final dimensions. Figure 40 shows a combination of aluminum members including (from top to bottom): upper web 90 degree angle connectors, lower web 90 degree angle connectors, and lower flange flat plate.



Figure 40: Processed aluminum members

4.5.4 Assembly

The prototype was assembled near the test frame. 153 Grade 8 steel bolts were hand tightened as the section was constructed. Minor hole misalignment occurred during the assembly process, but a quick boring with a cordless drill corrected any errors and removed minimal material. Figure 41 shows the prototype at various stages of assembly.



Figure 41: Prototype section at various stages of assembly

Once assembled the prototype was then craned into the test frame (Figure 42) and the support pin was inserted into the hinges. The support pin is a 1.8 m long, 76 mm diameter 4340 alloy steel rod. The complete mechanical test setup is outlined in Section 4.6.1.

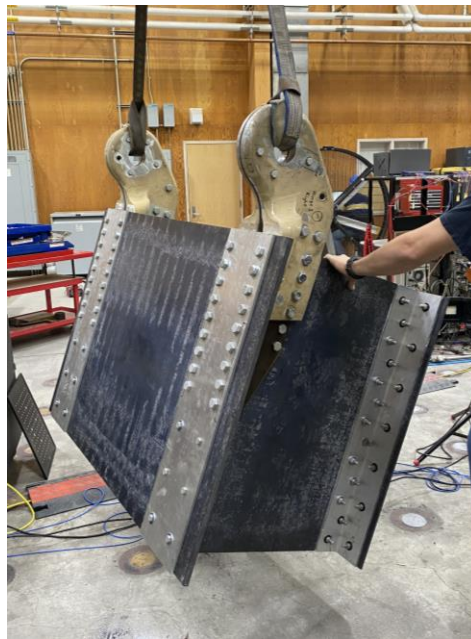


Figure 42: Prototype being craned into test frame

4.5.5 DIC Setup

It was determined that digital image correlation (DIC) would be used to track displacements on one face of the specimen. DIC was used earlier in this project to track strain fields as bearing coupons were deformed using a black and white painted speckle pattern. For this project it was determined that the most important data to obtain from testing was displacements, primarily in the vertical and out-of-plane directions. To achieve this goal, it was determined that point tracking dots would be used instead of the speckle pattern. The dots allow the two camera system to create point components in the calibrated volume, and track their relative movement. Additionally, they are easy to apply as they are a sticker component instead of a painted technique.

Two 12 MP Basler acA4112-30 um cameras with 12 mm Schneider Kreuznach 1.4/12-0906 lens were used. These allow for an image scale of 3.93 pixel/mm across the 1016 mm x 760 mm prototype surface area. The cameras were mounted to a piece of aluminum T-slot supported by a tripod. The cameras were spaced approximately 388 mm apart from each other and approximately 876 mm from the specimen. An additional light source was added near the cameras to illuminate the specimen's face. A photo of the DIC setup is seen in Figure 43 before the point trackers were applied.

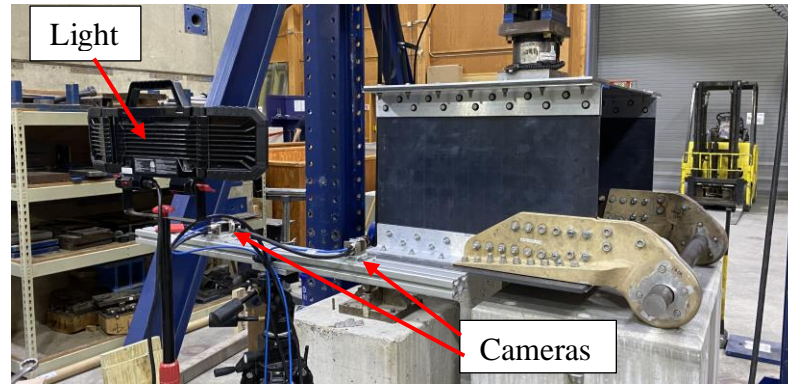


Figure 43: DIC system setup

It was determined that 3 mm dot sizes would be used based on the camera resolution and the specimen measuring volume. The aluminum and composite faces were painted black to minimize reflections. Trackers were adhered to the surface approximately every 50 mm along the width and 25 mm along the height. The entire surface was marked, as seen in Figure 44.

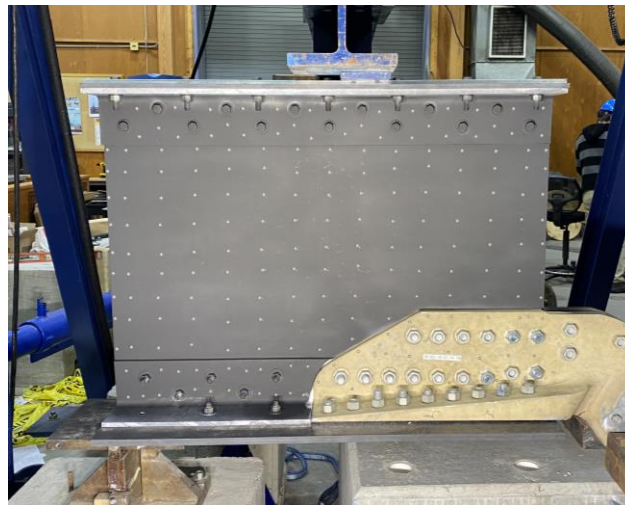


Figure 44: DIC face with point trackers

The cameras were then connected to the acquisition computer. Images were recorded using Streampix 8, triggered by a custom labview program. The labview program is able to trigger the cameras, as well as record analog position and load voltages from the test

frame. The programs acquired images and data at a rate of 2 Hz. The DIC cameras were then calibrated using a 1m calibration cross and noise was verified to be minimal.

4.6 Testing

Testing was performed on the structure in three phases. First, it was subjected to five 30 kN compressive loads as part of the mechanical testing. Second, it was inserted into an environmental chamber and subject to five 24 hour temperature cycles. Third, it was subjected to additional mechanical testing of varying compressive load levels. This section will detail experimental setups and observations from each round of testing.

4.6.1 Initial Mechanical Testing

The goal of the initial mechanical testing was to test the structure at a low load to provide a point of comparison to mechanical testing completed post thermal cycling. There was concern of premature failure if the structure were to exhibit a buckling response in the web. Euler buckling for composite structures was used per Equation 37.

$$\sigma_b = \frac{\pi^2 E_x}{\left(\frac{Kl}{r}\right)^2 + 1.2\pi^2 \frac{E_x}{G_{xz}}} \quad \text{Equation 37}$$

Where:

σ_b is the bearing stress

E_x is the bending modulus of elasticity in the x-direction

K is the end constraint factor ($K=1$ for pinned ends)

l is the length of the section

r is the radius of gyration (for a rectangular cross section $r = 0.289 \times \text{thickness}$)

G_{xz} is the bending shear stiffness in the through thickness direction

From laminate plate theory $E_x = 40.32$ GPa and $G_{xz} = 16.375$ GPa. Therefore, the critical buckling stress of the web was found to be 5.53 MPa, or a maximum load of 53.5 kN.

The structure contains two webs, therefore the buckling maximum load was predicted to be approximately 100 kN. However, in the event of uneven load distribution it was decided that only a load of 30 kN would be used for initial testing to guarantee survivability.

A CAD generated model of the mechanical test setup is shown in Figure 45. This setup was designed to mimic a three-point bend test. The load is applied by a 250 kN hydraulic actuator onto a steel I-beam. The I-beam spans both webs, allowing for load distribution to the webs. The specimen is supported on the front edge with a pin running through the hinges. The pin is supported on either side of the hinge with steel spacers. The rear supports are two 254 mm wide tilt tables that are centered to the webs. Concrete blocks are used to situate the structure at a working height.

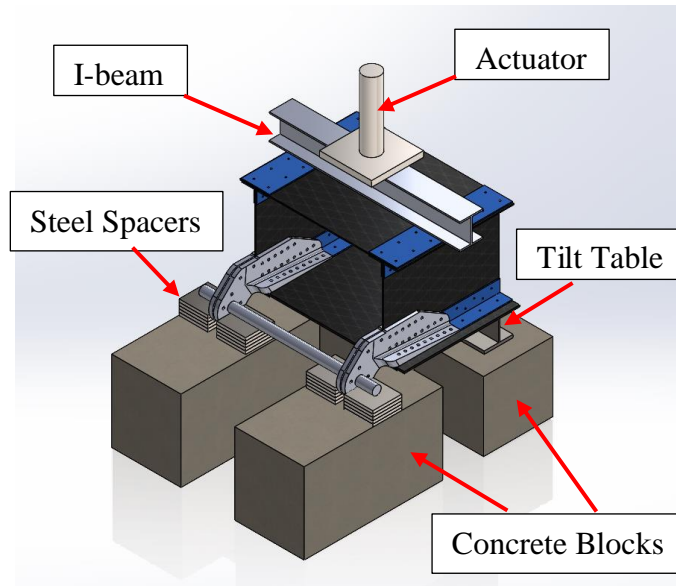


Figure 45: CAD model of test setup

Photos of the actual test setup are presented in Figure 46 where the left image is of the DIC face and the right is the truncated hinge face.



Figure 46: Actual test setup

The testing plan (Table 14) occurred in three phases as specified by the project sponsor. The first stage involves loading the structure to 30 kN at a rate of 5 kN/min. The load is

then held for 2 minutes, then released in a span of 1 minute. The test was repeated five times.

Table 14: Prototype load stages

Stage	Description	Time	Load (kN)
0	Hold at 0 load before test		0
1	Load up to 30 kN at a rate of 6 kN/min	5 min	30
2	Hold for 2 min	2 min	30
3	Unload structure at a rate of 30 kN/min	1 min	0

Testing occurred without incident and data was generated. Full experimental results will be discussed later in this chapter, but a graph of crosshead displacements vs load is shown in Figure 47.

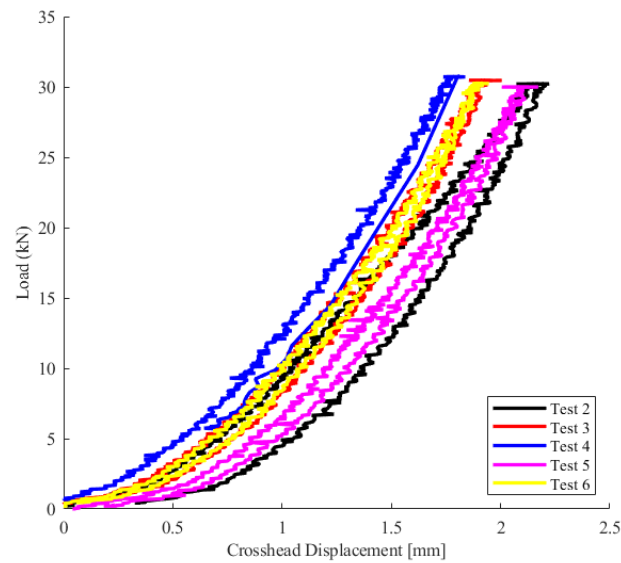


Figure 47: Crosshead displacement vs. load for initial 30 kN loadings

4.6.2 Temperature Cycling

Upon completion of mechanical testing the prototype was moved into an environmental chamber. Due to size limitations, the prototype had to be positioned vertically in the chamber. As no load was being applied to this structure during this stage of testing this was an acceptable configuration. The section positioned in the chamber is seen in Figure 48.



Figure 48: Specimen in environmental chamber

A 24-hour temperature and relative humidity cycle was developed with input from the project sponsors. Testing would involve reaching minimum and maximum temperatures and humidities. The complete cycle is shown in Figure 49.

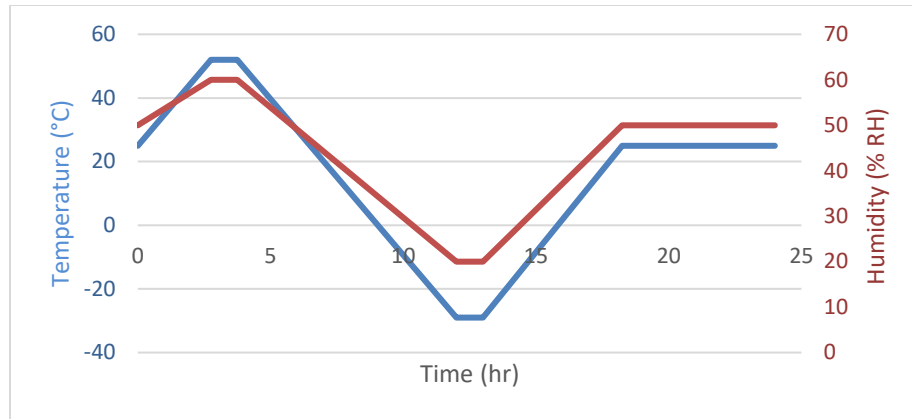


Figure 49: Temperature and humidity cycle

Actual temperature and relative humidity data is provided in Figure 50 and Figure 51 for Cycle 2 of the testing. All cycles followed similar curves. At low temperatures relative humidity is hard to control, as seen in the data. While the chamber was unable to achieve a low humidity the cycling is still valid as the temperature metrics, which are expected to produce the most specimen degradation, were achieved.

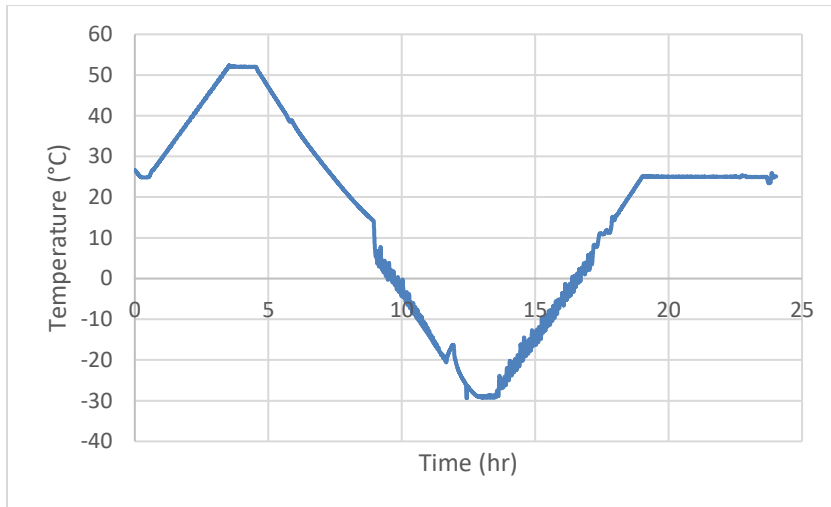


Figure 50: Temperature data for cycle 2

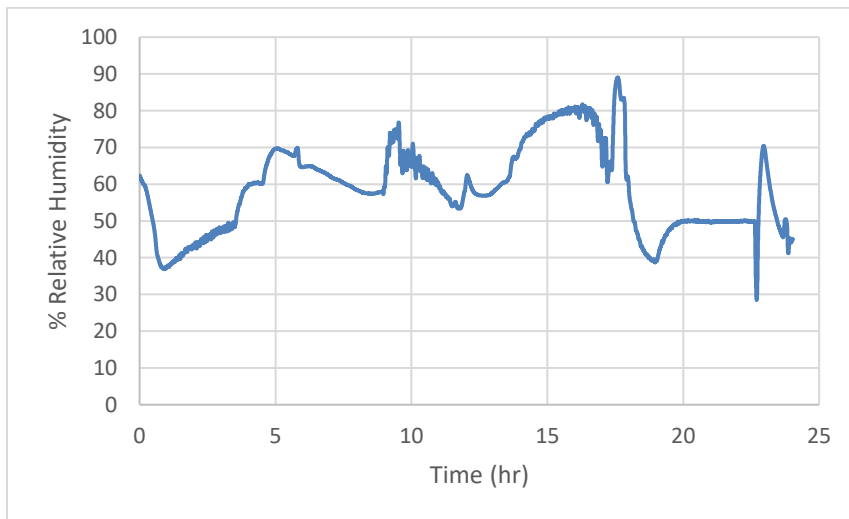


Figure 51: Humidity data for cycle 2

The specimen was inspected for damage between each temperature cycle. This included visually examining the specimen for any crack damage or other defects. All bolts were hand examined to make sure that they were still secure and would not spin when given a light torque. No damage or loosening was observed.

4.6.3 Secondary Mechanical Testing

After the specimen completed the thermal cycling it was repositioned back under the test frame. It was subject to the 30 kN load level again using the same load parameters specified before. The structure survived all five rounds of testing at 30 kN. It was determined that the structure would be tested at increasing load levels until either the structure failed or the capacity of the load frame was maximized. The additional load levels that were tested were: 60, 80, 100, 125, 150, 175, 200, and 210 kN. 210 kN was the maximum load that the frame could apply and the specimen did not fail at that level. For each load level five trials were run. All tests followed an 8 minute cycle as outlined in Section 4.6.1 where the load rates were adjusted to meet the required times. Crosshead average maximum displacements are reported in Table 15 for each load level. The load vs. crosshead displacement graphs for all five trials at 210 kN are shown in Figure 52.

Table 15: Mechanical testing cross head average maximum displacement

Load Level [kN]	Avg. Maximum Displacement [mm] (%COV)
30	1.83 (10.7)
60	2.79 (6.0)
80	3.74 (9.9)
100	3.51 (1.5)
125	3.98 (2.1)
150	4.43 (1.5)
175	4.88 (1.1)
200	5.32 (3.2)
210	5.47 (0.6)

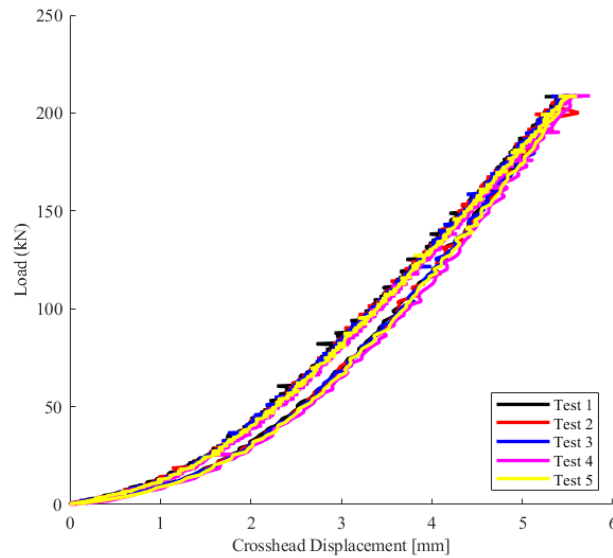


Figure 52: Crosshead displacement for final loading test (210 kN)

Testing concluded after reaching the maximum load that the test frame could apply. The setup was then dismantled and the composite panels and aluminum pieces were visually inspected for damage. No damage was observed around bolt holes, including no signs of bearing damage as experienced during the coupon testing.

4.7 Discussion of Experimental Results

Using the data obtained, four research objectives were identified for examination. First, a comparison of the structural response pre and post thermal cycling. Second, a study of the relative motion of the structure under loading. Third, an analysis of the out-of-plane motion and the potential for the web to buckle. Fourth, a comparison of the physical response of the structure to the predicted FEA model.

Displacement data from the DIC was calculated using GOM Correlate. These displacement trends were used to compare the structural response pre and post thermal

cycling. A point in the middle of the web was selected to be tracked across all 5 pre and 5 post temperature cycle tests. The resulting load vs. displacement graphs for this point are shown in Figure 53. No noticeable change in response due to thermal cycling is observed. Minor variations in maximum displacements may be caused by factors such as the specimen shifting in the test frame. Ideally, the specimen would have been tested to a higher level to capture the linear stiffness region. This would have allowed for a linear regression to be taken, and the resulting stiffnesses given by the line's slopes could be compared.

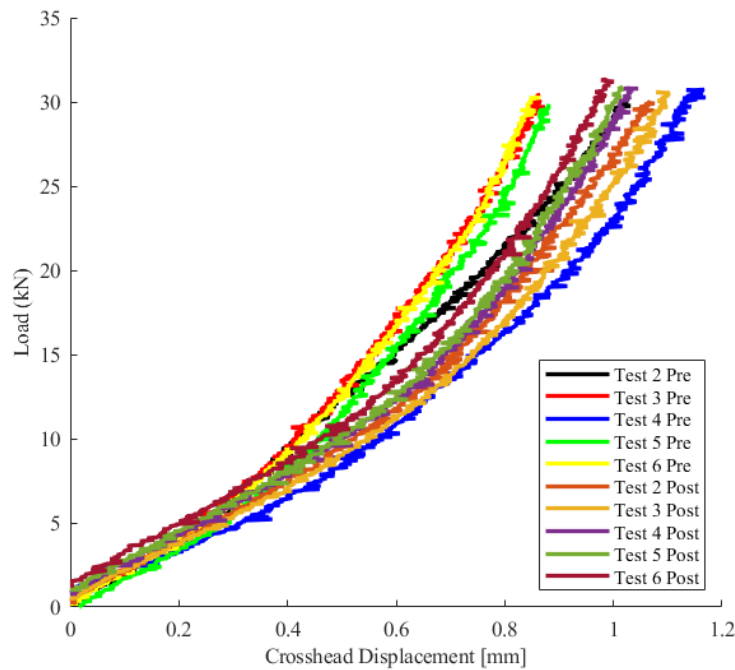


Figure 53: Pre and post temperature cycle comparison graph

As no major change was observed in the structure due to temperature cycling, an examination into degradation due to repeated loading was investigated. If the structure were to acquire damage during testing it is expected that there would be a change in

stiffness. The stiffness of the structure is defined as the slope of the linear region of the load vs. displacement curve. To capture the stiffness of the entire structure the load and displacement were taken at the cross head of the test frame. A linear regression was taken in the load range of 100-150 kN for loading levels of 150, 175, 200, and 210 kN. The resulting average stiffness across all five trials for each load case is summarized in Table 16. No major changes are observed in the stiffness between load levels. There was a minor drop in stiffness from 175 to 200 kN, but this may be due to other factors such as the structure slightly shifting in the test frame.

Table 16: Stiffness degradation of prototype

Load Level	Average Stiffness [kN/mm] (%COV)
150	49.73 (1.6)
175	49.84 (0.7)
200	49.10 (1.3)
210	49.08 (0.5)

Out of plane displacement was additionally examined to determine buckling failure of the structure. Using DIC data obtained during the testing runs at 210 kN an examination into the out of plane response could be conducted. Figure 54 shows the typical out of plane movement of the structure at maximum load. The rear edge of the structure is observed to deform the most. This is expected as the opposite edge is supported by the hinge which shortens the buckling length of the free edge. Failure of the panel is expected to occur at this location due to local buckling effects.

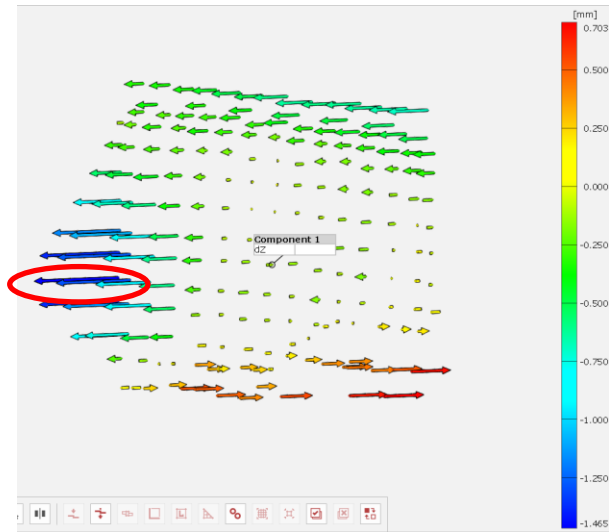


Figure 54: Out of plane motion peak under 210 kN loading

Load vs. displacement graphs were examined for this point of failure. The curves show a fairly linear trend as seen in Figure 55. As failure occurs the graph is expected to flatten as minimal load changes result in large deformation changes. As this is not seen in this graph it can be assumed that the structure could take on more load before experiencing buckling failure.

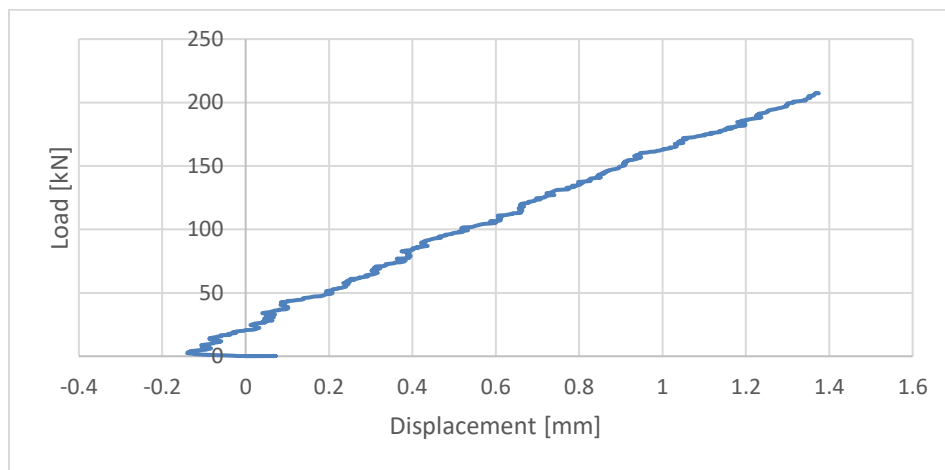


Figure 55: Out of plane motion vs. load under 210 kN loading

The DIC data was also used to examine how the structure deformed relative to itself. It was observed that the tilt table (left) side of the structure experienced much larger displacements than the hinge side. Figure 56 shows the maximum vertical displacements of the structure during a 210 kN load. The left side of the structure experiences approximately 1 mm more deflection than the right side. This is most likely due to the increased compliance of the tilt table.

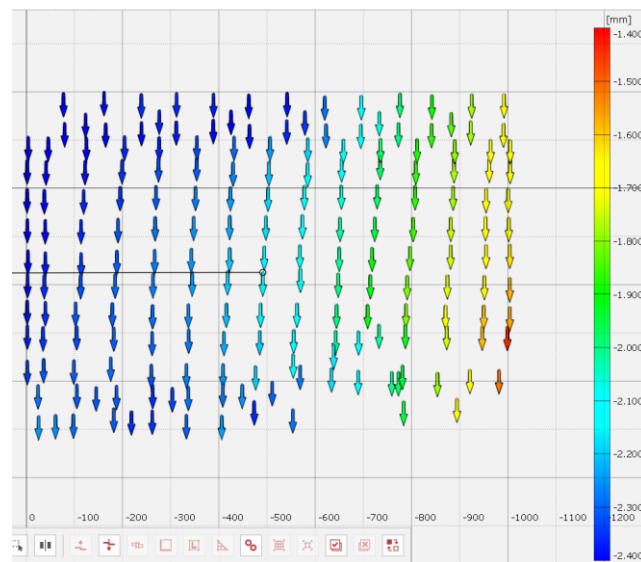


Figure 56: Vertical displacements at 210 kN of load

Figure 57 shows the horizontal movement of the structure under maximum loading. Surprisingly the structure shifts forward during testing. This shift may be due to a multitude of factors such as off centered loading and the potential for the specimen to slide on the tilt tables. Additionally it was noted that the bottom of the structure shifted more relative to the top. This may be due to proximity of the load application.

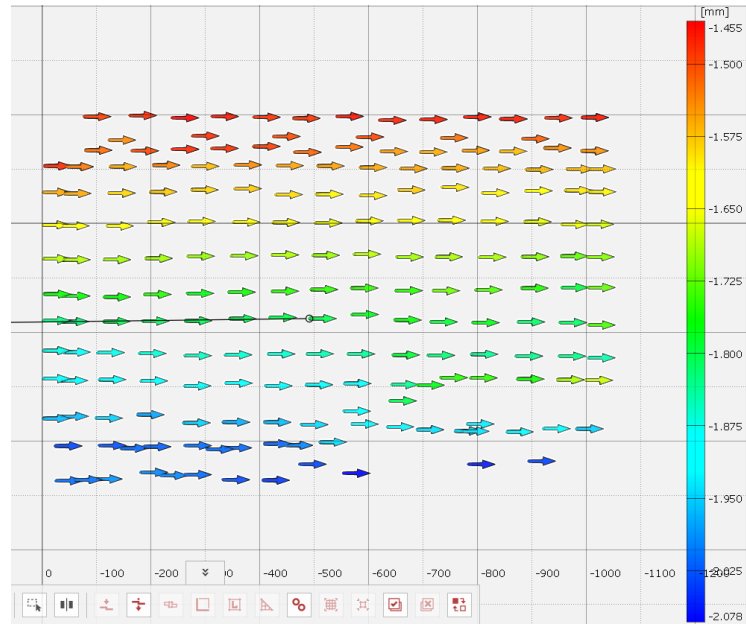


Figure 57: Horizontal displacement at 210 kN of load

Finally, comparing the prototype response to the FEA model the following observations are noted. At low load levels the mid-span deflection is slightly under-predicted by the FEA model (0.85 mm vs. observed 1.04 mm). However, at higher load levels the deflection is over-predicted by the FEA model (5.8 mm vs. observed 2.16 mm). While not ideal, this means that the FEA model is over conservative at high loads. Therefore, continued model refinement is required. Such areas that may be refined are redefinition of load application and added clamping forces at bolts due to induced torques.

4.8 Conclusion and Recommendations

The design, manufacturing and testing of a small scale continuous fiber reinforced thermoplastic composite structure was presented. Design constraints, theory, and analysis were specified for the structural design. A Matlab script was developed to allow for rapid comparisons between I-beam, double web I-beam and box beam sections using

Timoshenko beam theory. It was determined that a double web I-beam would be most advantageous due to its increased strength and rigidity. A T-style connector was then detailed to join the composite panels together to form the beam cross section. Due to feasibility issues the connector was modified to use readily available aluminum stock members.

Next, additional design verification took place using an Abaqus finite element model. Both full-scale and prototype scale models were developed. Designs were examined for failure using Tsai-Wu failure theory, as well as stress examinations around bolt holes.

Next, a small scale prototype was constructed. Challenges, such as the receipt of a truncated hinge, were overcome. The prototype section was then subject to three rounds of testing; mechanical, thermal, and then mechanical again. Low load testing was conducted before the thermal cycling to guarantee survivability and provide a point of reference. After thermal cycling, the section was tested at increasing load levels until the test frame was maximized. It was found that the temperature cycling did not seem to have any negative effects on the structure. Additionally, it was found that the stiffness of the structure did not degrade due to repeated and increasing loading. Finally, it was observed that out-of-plane motion was the greatest along the rear edge of the structure and that buckling failure would be most likely to occur there; however, it was never reached.

Based on the work done in this study the following recommendations are given:

- CFRTP CF/PPS double web I-beams provide great structure rigidity and strength and are easily assembled through modular construction techniques. Additional testing should be conducted to determine failure modes and strengths of similar structures using a variety of materials, geometry, connector styles and panel thicknesses.
- A continued effort and refinement of the understanding and modeling of interconnected composite structures using finite element analysis to better predict the displacement and failure of these structures is recommended.

CHAPTER 5: CONCLUSION AND RECOMMENDATIONS

5.1 Conclusions

This thesis presented research that was completed to better understand joining methods for continuous fiber reinforced thermoplastic composites in structural applications.

Tasked with developing a composite structure to replace an existing metallic structure, the following topics were explored and analyzed.

First, background research through a literature review was conducted to determine the optimal material for the project. A thermoplastic matrix was selected over a thermosetting one due to ease of manufacturability and recyclability. Five thermoplastic polymer matrices were selected for examination, PET, PETg, PP, PPS, and PC and two fiber reinforcement types, carbon (CF) and glass (GF). From these it was ultimately determined that carbon fiber reinforced PPS would be the most advantageous material due to its high strength and good environmental degradation properties.

Manufacturing methods were explored to generate small composite panels. Continuous fiber reinforced thermoplastic tapes were selected due to their ease of manufacturing and availability. A description of how the tapes are stacked to create a composite blank was given. The consolidation process was outlined and an emphasis on cooling rates for semi-crystalline polymers was presented. Two closed mold consolidation processes were discussed. Results from the first mold influenced the design of the second mold.

Ultimately, a closed steel mold that utilizes easily removable sides was selected to consolidate the panels needed for coupon level testing.

Next, research was conducted into joining methods for CFRTP composites. A literature review was presented that outlined the state of the art in thermoplastic composite joining methods. From these methods two were selected for experimental examination; bolted and adhesive joining. Bolted joints were evaluated using ASTM D5961 [41]. CF/PPS materials were obtained from two manufacturers to compare bearing responses. It was found that they both exhibited similar maximum bearing strengths; however, Material B had a much stiffer response than Material A (9.44 GPa vs. 5.41 GPa). Adhesive testing was completed according to ASTM D5868. Two adhesives were selected for investigation. A small study was done into increasing the surface free energy of the CF/PPS coupons to increase bondability using plasma treatments. This technique was successful and parameters of laboratory equipment were optimized. Adhesive lap shear testing yielded a preference for the film based adhesive. However, the maximum adhesive strength observed (18.3 MPa) was much less than that required for structural joints in this project. Therefore, it was decided that bolted joints would be used.

Finally, the development of a composite joint prototype was detailed. The underlying design theory and analysis was discussed, including the use of Timoshenko beam deflection assumptions and finite element models. An aluminum T-style connector was designed and modified to provide a method to construct thermoplastic beam sections. The manufacturing process of the prototype was outlined and a solution to receiving a truncated hinge was provided. The prototype was then tested in three rounds: compressive mechanical testing, thermal testing, and a second round of compressive mechanical testing. From these tests the following observations were noted:

- Thermal temperature cycling appeared to have no negative effect on the structural response of the prototype.
- The structure exhibited no change in stiffness due to repeated and increasing loading. This observed response was limited to the load capacity of the frame, but the structure was able to survive 210 kN without degradation.
- Out of plane motion was observed to be the greatest in the web at the rear free edge. If the structure were to fail it is believed that buckling failure would occur at this point.

As the load capacity of the test frame was reached, testing concluded for this research. Viability of joints in continuous fiber reinforced thermoplastic composites for use in structural applications was verified.

5.2 Recommendations for Future Work

Based on the findings in this study, future work on joining methods for large scale continuous fiber reinforced thermoplastic structures is recommended. Areas of interest are detailed in the following subsections.

5.2.1 Scalability

This research presented a prototype that was manufactured using a thermoforming process with a stamping press. This is a batch process that is suitable for prototyping and fast production of relatively small components (up to 1.5 m). However, a continuous forming process, such as thermoplastic pultrusion, is required to scale up parts for structural applications.

Similar to producing large scale thermoset composite parts, pultrusion has been identified as the optimal way to fabricate large continuous cross section members (lineal profiles). A paper published in 2021 by Minchenkov *et al.* [4] provides a review of the current state of the art in thermoplastic pultrusion. Thermoplastic pultrusion can be classified into reactive and nonreactive processes. Nonreactive processes use materials that are already polymerized such as commingled fibers or thermoplastic tapes, whereas reactive processes impregnate the fibers in the forming process. Figure 58 shows a typical nonreactive pultrusion setup, and Figure 59 shows a reactive pultrusion setup.

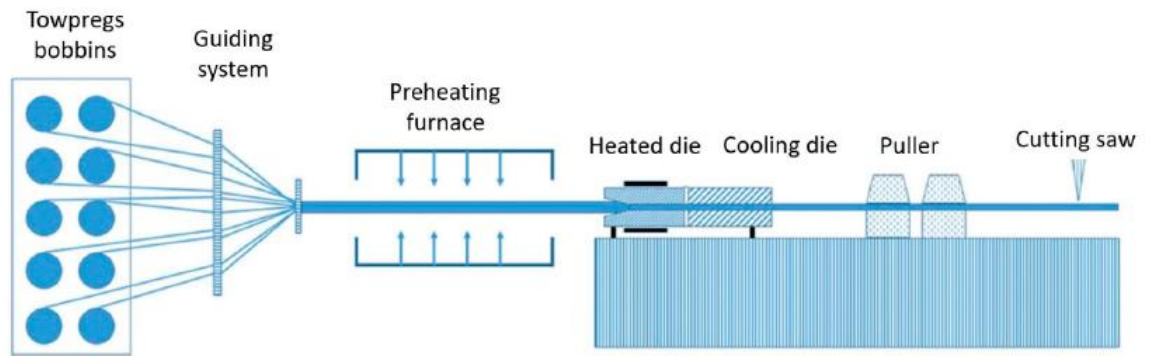


Figure 58: Nonreactive Pultrusion Line. [4]

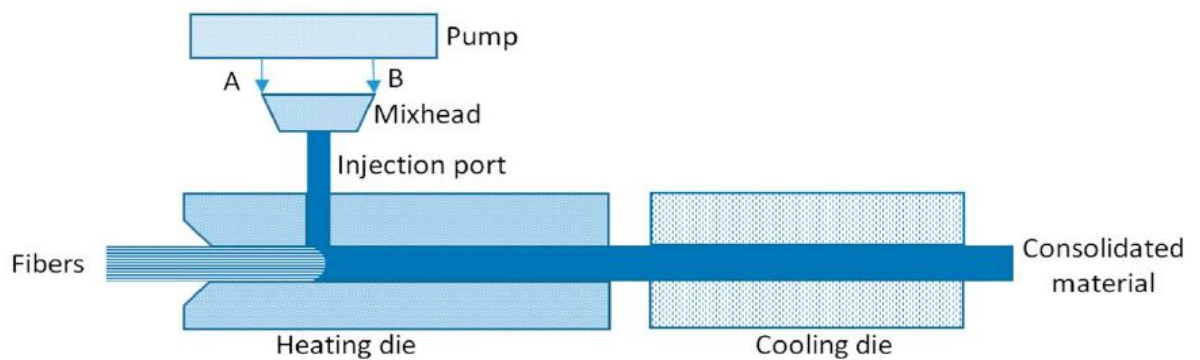


Figure 59: Reactive Pultrusion Line. [4]

While nonreactive pultrusion can use any commingled or tape thermoplastic, reactive pultrusion is typically limited to polycarbonates (PC), polyesters (PE), polyurethanes (PU), polymethylmethacrylates (PMMA), and polyamides (PA) (in particular PA-6).

The general process of nonreactive pultrusion is that the input material is heated to a temperature close to the polymer melt temperature. Then the material is pulled through a heated die. The die typically has a slight taper, and in some processes, there may be multiple dies used to shape the member. Following the heated die, the material is cooled in a cooling die. There has been extensive work in optimizing the parameters of this process, such as selection of heating and cooling methods, temperature optimization, pulling speed, pulling force, etc. However, this manufacturing process is still being developed and more research is needed.

Additionally, this pultrusion manufacturing research should focus on the crystallization of the polymer, as well as the quality of the parts. Crystallization should be assessed through additional DSC testing as well as laboratory coupon testing for varying cooling rates. Part quality should be examined using nondestructive testing such as thermography [46], thermos-tomography [47], C-scan [48], or ultrasonic void detection [49].

5.2.2 Optimization/modeling

The prototype beam section developed for this research primarily relied on utilizing existing design geometry from the existing metallic structure. This was done to simplify design decisions and to make the structure compatible with other subsystems linked to

the structure, such as hydraulics, decking, etc. Future work can be done to optimize geometry to take full advantage of the unique strengths and properties of CFRTP composites. Areas of optimization include: fiber positioning, composite panel thickness, and beam cross-sectional geometry. By optimizing these conditions significant weight savings could be achieved, decreasing material, labor, and maintenance costs.

5.2.3 Hybrid laminates

The potential of developing hybrid, multi-fiber type laminates as a way to decrease costs of CFRTP composites is presented. As stated earlier carbon fibers are relatively expensive compared to fibers such as glass. As the CFRTP tape market continues to expand many manufacturers are developing tapes that utilize the same polymer matrix but contain different fibers. This presents a way to lay up a laminate where the exterior faces could be carbon fiber and the interior core could be glass reinforced. As all tapes contain the same base polymer the consolidation will yield a plate with good inter-layer adhesion. As glass fibers are heavier than carbon and have slightly lower strength, the CFRTP structure must be optimized for cost, strength, and weight.

5.2.4 Full Scale Structural Beam

The final recommendation for future research is development of a full scale structural CFRTP beam. Limitations of this research include the inability to simulate all forces developed on and in the structure due to its decreased length and available hardware. The lack of the upper hinges prevented additional displacement constraints that may have influenced how the structure deformed. Additionally, the testing performed on the

prototype did not allow for the development of compressive and tensile forces in the upper and lower flanges of the structure. Therefore, it is recommended that after the structure is optimized using the recommended work discussed in the previous sections, a full scale beam should be tested.

REFERENCES

- [1] C. Seigars, "Feasability of Hybrid Thermoplastic Composite-Concrete Load Bearing System," University of Maine, Orono, ME, 2018.
- [2] S. R., "Automotive composites offer lighter solutions," *Reinforced Plastics*, vol. 54, no. 2, pp. 22-28, 2010.
- [3] e. a. Laraib Alam Khan, "Cost-effective manufacturing process for the development of automotive from energy efficient composite materials and sandwich structures," *Polymer Composites*, vol. 35, no. 1, pp. 97-104, 2014.
- [4] K. Minchenkov, "Thermoplastic Pultrusion: A Review," *Polymers*, vol. 13, no. 180, 2021.
- [5] A. R. Offringa, "Thermoplastic composites—rapid processing applications," *Composites Part A: Applied Science and Manufacturing*, vol. 27, no. 4, pp. 329-336, 1996.
- [6] E. R. Larson, *Thermoplastic Material Selection: A Practical Guide*, Elsevier Science & Technology Books, 2015.
- [7] R. Walsh, "A comparative assesment of bolted joints in a graphite reinforced thermoset vs. thermoplastic," *Composites*, vol. 21, no. 2, 1990.
- [8] Annonymous, "Surface Treatments for adhesive bonding: Thermoset vs thermoplastic," *CompositesWorld*, vol. 6, no. 8, pp. 18-21, 2020.
- [9] D. Quan, "Rapid surface activation of carbon fibre reinforced PEEK and PPS composites by high-power UV-irradiation for the adhesive joining of dissimilar materials," *Composites Part A*, vol. 137, 2020.
- [10] J. Bozzelli, "Melting Amorphous vs. sem-crystalline Plastics," *Plastics Technology*, vol. 68, no. 1, pp. 30-33, 2022.
- [11] J. S. H. Moshe M. Domb, "The Effect of Cooling Rate on Free-Edge Stress Development in Semi-Crystalline Thermoplastic Laminates," *Journal of Composite Materials*, vol. 32, no. 4, pp. 361-385, 1998.

- [12] "Differences between commodity and engineering plastics," Plasticut, [Online]. Available: <https://www.plasticut.com.au/differences-between-commodity-engineering-plastics/>. [Accessed 5 November 2021].
- [13] T. Technologies, *Thermoplastic Classification Table*.
- [14] P. Zuo, "Multiscale physicochemical characterization of a short glass fiber–reinforced polyphenylene sulfide composite under aging and its thermo-oxidative mechanism," *Polymers Advanced Technologies*, vol. 30, no. 3, pp. 584-597, 2018.
- [15] p. Zuo, "Multi-scale analysis of the effect of loading conditions on monotonic and fatigue behavior of a glass fiber reinforced polyphenylene sulfide (PPS) composite," *Composites Part B: Engineering*, vol. 145, pp. 173-181, 2018.
- [16] M. Paula, "Characterization of SixOyNz coating on CF/PPS composites for space applications," *Surface and Coatings Technology*, vol. 335, pp. 159-165, 2017.
- [17] F. v. H. Thomas de Bruijn, "Rotorcraft access panel from recycled carbon PPS – The world's first flying fully recycled thermoplastic composite application in aerospace," *Reinforced Plastics*, vol. 65, no. 3, pp. 148-150, 2021.
- [18] J. Thomason, "Glass Fibre sizing: a review," *Composites Part A: Applied Science and Manufacturing*, vol. 127, 2019.
- [19] J. M. F. d. P. M. C. R. Clara Leal Nogueira, "Effect of the Interfacial Adhesion on the Tensile and Impact Properties of Carbon Fiber Reinforced Polypropylene Matrices," *Materials Research*, vol. 8, no. 1, pp. 81-89, 2005.
- [20] H. L. e. al., "Interfacial adhesion and shear behaviors of aramid fiber/polyamide 6 composites under different thermal treatments," *Polymer Testing*, vol. 81, 2020.
- [21] B. Soares, "Mechanical behavior of basalt fibers in a basalt-UP composite," *Procedia Structural Integrity*, vol. 1, pp. 82-89, 2016.
- [22] R. S. P. e. al., "Development of basalt fiber-reinforced thermoplastic composites and effect of PE-g-MA on composites," *Polymer Composites*, vol. 38, no. 12, pp. 2798-2805, 2017.

- [23] O. B. C. F. Christoph Unterweger, "Synthetic fibers and thermoplastic short-fiber-reinforced polymers: Properties and characterization," *Polymer Composites*, vol. 35, no. 2, pp. 227-236, 2014.
- [24] D. Didier, "Heat transfer analytical models for the rapid determination of cooling time in crystalline thermoplastic injection molding and experimental validation," in *AIP Conference Proceedings*, 2018.
- [25] "Thermal Expansion - Linear Expansion Coefficients," The Engineering Toolbox, [Online]. Available: https://www.engineeringtoolbox.com/linear-expansion-coefficients-d_95.html. [Accessed 21 December 2021].
- [26] X. Cheng, "Effect of Damage on Failure Mode of Multi-Bolt Composite Joints Using Failure Envelope Method," *Composite Structures*, no. 160, pp. 8-15, 2017.
- [27] Y. Xiao, "Bearing strength and failure behavior of bolted composite joints (part I: Experimental investigation)," *Composites Science and Technology*, vol. 65, pp. 1022-1031, 2005.
- [28] J.-I. Choi, "Failure load prediction of composite bolted joint with clamping force," *Composite Structures*, vol. 189, pp. 247-255, 2018.
- [29] M. McCarthy, "Bolt-hole clearance effects and strength criteria in single-bolt, single-lap, composite bolted joints," *Composites Science and Technology*, vol. 62, pp. 1415-1431, 2002.
- [30] T. Yilmaz, "Investigation of load bearing performances of pin connected carbon/polyphenylene sulphide composites under static loading conditions," *Materials & Design*, vol. 28, no. 2, pp. 520-527, 2007.
- [31] A. Dickson, "Enhancing the bearing strength of woven carbon fibre thermoplastic composites through additive manufacturing," *Composite Structures*, vol. 212, pp. 384-388, 2019.
- [32] e. a. Markus Schweizer, "Adhesive bonding of CFRP: a comparison of different surface pre-treatment strategies and their effect on the bonding shear strength," *Journal of Adhesion Science and Technology*, vol. 31, no. 23, pp. 2581-2591, 2017.

- [33] e. a. Gennaro Scarselli, "Adhesion Improvement of Thermoplastics-Based Composites by Atmospheric Plasma and UV Treatments," *Applied Composite Materials*, vol. 28, pp. 71-89, 2021.
- [34] "What adhesive types are best for bonding composites?," Permabond, [Online]. Available: <https://www.permabond.com/resource-center/adhesive-types-bonding-composites/>. [Accessed 15 9 2021].
- [35] J.-H. Kweon, "Failure of carbon composite-to-aluminum joints with combined mechanical fastening and adhesive bonding," *Composite Structures*, vol. 75, no. 1-4, pp. 192-184, 2006.
- [36] e. a. C.-J. Lee, "Design of hole-clinching process for joining of dissimilar materials – Al6061-T4 alloy with DP780 steel, hot-pressed 22MnB5 steel, and carbon fiber reinforced plastic," *J Mater Process Technol*, vol. 214, no. 10, pp. 2169-2178, 2014.
- [37] S. J. R. J. T. Xianghu, "Effects of Cr plating layer on shear strength and interface bonding characteristics of mild steel/CFRP joint by laser heating," *Acta Metall Sin*, vol. 49, no. 6, pp. 751-756, 2013.
- [38] e. a. J. Esteves, "Friction spot joining of aluminum AA6181-T4 and carbon fiber-reinforced poly (phenylene sulfide): effects of process parameters on the microstructure and mechanical strength," *Materials and Design*, vol. 66, pp. 437-445, 2015.
- [39] e. a. K. Nagatsuka, "Direct joining of carbon-fiber-reinforced plastic to an aluminum alloy using friction lap joining," *Composites B Engineering*, vol. 73, pp. 82-88, 2015.
- [40] e. a. A. Prarmanik, "Joining of carbon fibre reinforced polymer (CFRP) composites and aluminium alloys – A review," *Composites Part A: Applied Science and Manufacturing*, vol. 101, pp. 1-29, 2017.
- [41] ASTM, ASTM D5961: Standard test method for bearing response of polymer matrix composite laminates, West Conshohocken, PA: ASTM International, 2017.
- [42] "ASTM D5868: Standard Test Method for Fiber Reinforced Plastic (FRP) Bonding," ASTM International, West Conshohocken, PA, 2014.

- [43] N. e. a. Pandiyaraj K., "Adhesive properties of polypropylene (PP) and polyethylene terephthalate (PET) film surfaces treated by DC glow discharge plasma.," *Vacuum*, vol. 83, no. 2, pp. 332-339, 2008.
- [44] B. B. & F. Guild, "Forced air plasma treatment for enhanced adhesion of polypropylene and polyethylene," *Journal of Adhesion Science and Technology*, vol. 27, no. 24, pp. 2714-2726, 2013.
- [45] J. Lee, "The structural characteristic of a polymer composite cellular box beam in bending," *Construction and Building Materials*, vol. 9, no. 6, pp. 333-340, 1995.
- [46] S. oiccardi, "Infrared thermography to evaluate thermoplastic composites under bending load," *Composite Structure*, vol. 134, pp. 900-904, 2015.
- [47] A. Huber, "Automated NDT inspection based on high precision 3-D Thermo-Tomography model combined with engineering and manufacturing data," *Procedia CIRP*, vol. 85, pp. 321-328, 2019.
- [48] B. Olson, "The Effects and Non-Destructive Evaluation of Defects in Thermoplastic Compression-Loaded Composite Cylinders," *Journal of Thermoplastic Composite Materials*, vol. 8, no. 1, 1995.
- [49] D. Saenz-Castillo, "Effect of processing parameters and void content on mechanical properties and NDI of thermoplastic composites," *Composites Part A*, vol. 121, pp. 308-320, 2019.
- [50] K. Minchenkov, "Thermoplastic Pultrusion: A Review," *Polymers*, vol. 13, no. 180, p. 180, 2021.
- [51] C. Seigars, "Feasability of Hybrid Thermoplastic Composite-Concrete Load Bearing System," University of Maine, Orono, 2016.

APPENDIX A

PRELIMINARY CAE VALUES – CONFIDENTIAL NOT TO BE DISCLOSED WITHOUT NDA

Celstran® CFR-TP PPS-CF60-01

General Description: Celstran® CFR-TP PPS CF60-01 is a 60% carbon fiber by weight PPS (polyphenylene sulfide) continuous fiber (uni-directional) reinforced thermoplastic composite tape. This material exhibits a high strength-to-weight ratio, excellent chemical and FST performance, and long-term heat stability. It is well suited for aerospace, oil/gas, sporting goods and industrial applications where demanding weight, chemical and FST performance is necessary.

Property	Value	Unit	Value	Unit
Polymer	PPS			
Fiber Type	Carbon			
Density	0.0549	lb/in ³	1.520	g/cm ³
Fiber Content	60	% by wt.		
Fiber Volume	53	% by vol.		
Tape Thickness*	0.0055	in	0.14	mm
Tape Width*	10.4	in	263	mm
Tape Areal Weight	6.9	oz/yd ²	235	g/m ²
Fiber Areal Weight	4.1	oz/yd ²	141	g/m ²

*Alternate tape widths and thicknesses may be available

		Property	Value	Unit	Value	Unit	Test Method
0° Unidirectional Mechanical Properties	Panel Tensile	Strength	286	ksi	1972	MPa	D3039
		Modulus	16.5	Msi	114	GPa	D3039
		Strain to Fail	1.78	%	1.78	%	D3039
		Poisson's Ratio (12)	0.341		0.341		D3039
	Flexural	Strength	177	ksi	1221	MPa	D7264
		Modulus	15.2	Msi	105	GPa	D7264
		Strain to Fail	1.20	%	1.20	%	D7264
	Compression	Strength	130	ksi	897	MPa	D6641
		Modulus	16.0	Msi	110	GPa	D6641
		Strain to Fail	0.70	%	0.70	%	D6641
		Poisson's Ratio (12)	0.298		0.298		D6641
	Tape Tension	Strength	295	ksi	2034	ksi	D3039M
Modulus		14.6	Msi	101	Msi	D3039M	
Strain to Fail		1.79	%	1.79	%	D3039M	

Celstran® CFR-TP PPS-CF60-01

8-24-2015



ENGINEERED MATERIALS
celanese.com/engineered-materials

Contact Information

Americas
8040 Dixie Highway
Florence, KY 41042 USA
Product Information Service
t: +1-800-833-0882 f: +1-859-372-3214
Customer Service
t: +1-800-525-9960 f: +1-859-372-3214
e: info-enr@celanese.com

Europe
Am. Unisys-Park 1
65843 Sulzbach, Germany
Product Information Service
t: +49-603-85427-531
f: +49-603-854009-1011
e: info-engineeredmaterials-eu@celanese.com

Asia
456D Jinko Road, Zhang Jiang Hi Tech Park
Shanghai 201203 P.R.C.
Customer Service
t: +86 21 3861 9266
f: +86 21 3861 9399
e: info-engineeredmaterials-asia@celanese.com

© 2014 Celanese or its affiliates.
All rights reserved.

This publication was printed based on Celanese's present state of knowledge, and Celanese undertakes no obligation to update it. Because conditions of product use are outside Celanese's control, Celanese makes no warranties, express or implied, and assumes no liability in connection with any use of this information. Nothing herein is intended as a license to operate under or a recommendation to infringe any patents.

Celanese® registered C-ball design and all other trademarks identified herein with ®, TM, SM, unless otherwise noted, are trademarks of Celanese or its affiliates.

	Property	Value		Unit		Test Method	
90° Unidirectional Mechanical Properties	Tensile	Strength	3.29	ksi	22.7	MPa	D3039
		Modulus	1.16	Msi	8.02	GPa	D3039
		Strain to Fail	0.273	%	0.273	%	D3039
		Poisson's Ratio (21)	0.0879		0.0879		D3039
		Poisson's Ratio (23)	0.527		0.527		D3039
	Flexural	Strength	3.80	ksi	26.2	MPa	D7264
		Modulus	0.838	Msi	5.78	GPa	D7264
		Strain to Fail	0.486	%	0.486	%	D7264
	Compression	Strength	14.6	ksi	101	MPa	D6641
		Modulus	1.15	Msi	7.93	GPa	D6641
		Strain to Fail	1.39	%	1.39	%	D6641
		Poisson's Ratio (21)	--		--		D6641

Contact Information

Americas
8040 Dixie Highway
Florence, KY 41042 USA
Product Information Service
t: +1-800-833-4882 t: +1-859-372-3244
Customer Service
t: +1-800-526-4960 t: +1-859-372-3214
e: info-engineeredmaterials-am@celanese.com

Europe
Am Unisys-Park 1
65843 Sulzbach, Germany
Product Information Service
t: +(00)-800-86427-531
t: +49-(0)-69-45009-1011
e: info-engineeredmaterials-eu@celanese.com

Asia
4560 Jinke Road, Zhang Jiang Hi Tech Park
Shanghai 201203 PRC
Customer Service
t: +86 21 3861 9266
t: +86 21 3861 9599
e: info-engineeredmaterials-asia@celanese.com

	Property	Value		Unit		Test Method	
Shear Mechanical Properties	Double V-notched	G ₁₂ Strength	6.25	ksi	43.1	MPa	D5379
		G ₁₂ Modulus	0.499	Msi	3.44	GPa	D5379
		G ₁₂ Strain to Fail	5.00	%	5.00	%	D5379
		G ₂₃ Strength	--	ksi	--	MPa	D5379
		G ₂₃ Modulus	--	Msi	--	GPa	D5379
		G ₂₃ Strain to Fail	--	%	--	%	D5379
	+/- 45°	G ₁₂ Strength	6.803	ksi	46.9	MPa	D3518
		G ₁₂ Modulus	0.447	Msi	3.08	GPa	D3518
		G ₁₂ Strain to Fail	5.00	%	5.00	%	D3518
	Interlaminar	Shear Strength	--	ksi	--	MPa	DNT
		Shear Modulus	--	Msi	--	GPa	DNT
		Shear Strength	--	ksi	--	MPa	DNC
		Shear Modulus	--	Msi	--	GPa	DNC

© 2014 Celanese or its affiliates.
All rights reserved.

This publication was printed based on Celanese's present state of knowledge, and Celanese undertakes no obligation to update it. Because conditions of product use are outside Celanese's control, Celanese makes no warranties, express or implied, and assumes no liability in connection with any use of this information. Nothing herein is intended as a license to operate under or a recommendation to infringe any patents.

Celanese® registered C-ball design and all other trademarks identified herein with ®, TM, SM, unless otherwise noted, are trademarks of Celanese or its affiliates.

Celstran® CFR-TP PPS-CF60-01

PRODUCT DATA SHEET

DESCRIPTION

Toray Cetex® TC1100 is a high-end but cost-effective thermoplastic composite material, utilizing a semi-crystalline PPS polymer for excellent mechanical properties and an outstanding chemical and solvent resistance.

With over 7 million parts in flight and qualified for structural application at Airbus, Boeing, and many other airframe OEMs, Toray Cetex® TC1100 offers a great balance between cost and performance, both mechanical and chemical. The material is inherently flame resistant (< 35/35 OSU) with low smoke emission.

Besides application in aerospace, Toray Cetex® TC1100 is often the material of choice for demanding industrial applications.

Toray Cetex® TC1100 is available as a UD tape, a fabric prepreg, and as reinforced thermoplastic laminates (RTLs) of varying thicknesses. RTLs can be equipped with lightning strike protection, and carbon reinforced RTLs can be supplied with a thin glass top layer to protect a partly metallic assembly against galvanic corrosion.

FEATURES

- ▶ Qualified and certified to aerospace OEM specifications
- ▶ Outstanding performance-to-cost ratio
- ▶ Service temperature can exceed T_g depending on part design
- ▶ Lightning strike material as well as galvanic corrosion protection can be incorporated on laminates
- ▶ Inherently flame retardant
- ▶ Outstanding chemical and solvent resistance
- ▶ Indefinite shelf life at ambient temperature storage

PRODUCT TYPE

PPS (PolyPhenyleneSulfide) Thermoplastic Resin System

TYPICAL APPLICATIONS

- ▶ Primary and secondary aircraft structures: wing leading edges, engine pylon structures, clips and cleats for fuselage structure
- ▶ Aircraft interiors: acoustic structures, structural components of seats, galleys, stowage boxes
- ▶ High-end industrial applications where corrosive environments, dimensional stability, or vibration dampening play a role

TYPICAL NEAT RESIN PROPERTIES

Density (specific gravity)	1.35 g/cm ³ (84.3 lb/ft ³)
T_g (glass transition)	90°C (194°F)
T_m (melt)	280°C (536°F)
T_p (processing)	300–330°C (570–625°F)

MAIN QUALIFICATIONS

- ▶ ABS 5045
- ▶ ABS 5222
- ▶ MEP 15-052
- ▶ NTA 62901 (Type II)

SHELF LIFE

Out Life:	Indefinite at ambient temperature storage
Frozen Storage Life:	Not applicable—product does not require freezing



Contact us for more information:

North America/Asia/Pacific
 e explore@toraytac-usa.com
 t +1 408 465 8500

Europe/Middle East/Africa
 e explore@toraytac-europe.com
 t +33 (0)548 633 933

TC1100_POS_v5_2019-11-20
 Page 1/6

PRODUCT DATA SHEET

Continued from page 2

Standard Modulus T300JB 3K Carbon 290gsm FAW 5HS Woven Fabric Reinforced Laminate 43% RC				
Property	Condition	Test Method	Results	
Tensile Strength 0°	ETW*	EN 2597 B	736 MPa	107 ksi
Tensile Modulus 0°	ETW*	EN 2597 B	56.0 GPa	8.1 Msi
Tensile Strength 90°	ETW*	EN 2597 B	818 MPa	119 ksi
Tensile Modulus 90°	ETW*	EN 2597 B	56.0 GPa	8.1 Msi
Compression Strength 0°	ETW*	EN 2850 B	522 MPa	76 ksi
Compression Modulus 0°	ETW*	EN 2850 B	52.0 GPa	7.5 Msi
Compression Strength 90°	ETW*	EN 2850 B	481 MPa	70 ksi
Compression Modulus 90°	ETW*	EN 2850 B	52.0 GPa	7.5 Msi
In-Plane Shear Strength ±45°	ETW*	AITM 1-0002	112 MPa	16 ksi
In-Plane Shear Modulus ±45°	ETW*	AITM 1-0002	2.7 GPa	0.4 Msi
Flexural Strength 90°	ETW*	EN 2562 A	743 MPa	108 ksi
Flexural Modulus 90°	ETW*	EN 2562 A	44.0 GPa	6.4 Msi
Compression After Impact Strength	ETW*	AITM 1-0010, issue 3	220 MPa	32 ksi

50% fiber by volume (Vf)
 *ETW is tested at 80°C (176°F)/dry after 1000 hours of conditioning at 70°C (158°F)/85% RH

Standard Modulus Carbon Z21gsm FAW UD Tape Laminate 34% RC				
Property	Condition	Test Method	Results	
Tensile Strength 0°	RTD	ASTM D 3039	2020 MPa	294 ksi
Tensile Modulus 0°	RTD	ASTM D 3039	134 GPa	19.5 Msi
Tensile Strength 90°	RTD	ASTM D 3039	39 MPa	5.7 ksi
Tensile Modulus 90°	RTD	ASTM D 3039	10 GPa	1.4 Msi
Compressive Strength 0°	RTD	ASTM D 6641	1100 MPa	160 ksi
Compressive Modulus 0°	RTD	ASTM D 6641	117 GPa	17 Msi
In-Plane Shear Strength ±45°	RTD	ASTM D 3518	82 MPa	11.9 ksi
In-Plane Shear Modulus ±45°	RTD	ASTM D 3518	3.5 GPa	0.5 Msi
Flexural Strength 90°	RTD	ASTM D 7264	68 MPa	9.9 ksi
Open-Hole Compressive Strength	RTD	ASTM D 6484	267 MPa	38.7 ksi
Compression After Impact Strength 30.5 J (270 in/lb) Impact Energy	RTD	ASTM D 7137	216 MPa	31.4 ksi

Fiber type AS4A
 59% fiber by volume (Vf)

APPENDIX B

```
%% Timoshenko Beam Deflection Calculator
% By Andrew Moran

%% -----Input Lamina and Geometry Parameters-----
-----

%Laminate Input
ThetaNonSym_Top = [0;0;0;0;45;-45;90;0;0;45;-45;90;0;0;45;-
45;90;0;0;45;-45;90;0;0;45;-45;90;0;0;0;0;0;0];
ThetaNonSym_Bot = [0;90;45;-45;0;90;45;-45;0;90;45;-45;0;90;45;-
45;0;90;45;-45;0;90;45;-45;0;90;45;-45;0;90];
ThetaNonSym_Web = [0;0;0;0;45;-45;90;0;0;0;45;-45;90;0;0;0;45;-
45;90;0;0;0;45;-45;90;0;0;0;45;-45;90;0;0;0;45;-
45;90;0;0;0;45;-45;90;0;0;0;0;0;0;0];

%Make Laminate Symmetric
ThetaArray_Top = MakeSymmetric(ThetaNonSym_Top);
ThetaArray_Bot = MakeSymmetric(ThetaNonSym_Bot);
ThetaArray_Web = MakeSymmetric(ThetaNonSym_Web);

%import material properties for PPS
E1 = 114e9; %Pa
E2 = 8.02e9; %Pa
nu12 = 0.341;
G12 = 3.44e9; %Pa
h = 0.14e-3; %mm

%import material properties for C-LA 1812
%E1 = 89.22e9; %Pa
%E2 = 6.88e9; %Pa
%nu12 = 0.355;
%G12 = 3.992e9; %Pa
%h = 0.722e-3; %mm

%Beam Cross Section Geometry Input
%Beam Type 1 = I Beam
%Beam Type 2 = Double Web I-Beam
%Beam Type 3 = Box Beam

BEAM_TYPE = 2;

Top_Flange_Width = convlength(10+3/8, 'in', 'm'); %m
Top_Flange_Thickness = length(ThetaArray_Top)*h; %m
Web_Height = convlength(29, 'in', 'm'); %m
Web_Thickness = length(ThetaArray_Web)*h; %m
Bottom_Flange_Width = convlength(14+3/8, 'in', 'm'); %m
Bottom_Flange_Thickness = length(ThetaArray_Bot)*h; %m

Box_Beam_Vertical_Thickness = length(ThetaArray_Web)*h; %m
Box_Beam_Horizontal_Thickness = length(ThetaArray_Top)*h; %m
Box_Beam_Outer_Height = 1; %m
```

```

Box_Beam_Outer_Width = 0.75; %m

%Load Defenitions
%Bridge Length L
L = 19-1.5; %m %assuming 0.75m banking
%MLC 120 Length
L_MLC_120 = 6.1; %m
%MLC 120 Distributed Load with 1.2 Impact Factor
Impact_Factor = 1.2;
m_MLC_120 = 1067.55e3; %N
q_MLC_120 = m_MLC_120*Impact_Factor/(2*L_MLC_120); %N/m per beam
%Mud Distributed Load
q_Mud = 2370; %N/m

%% ----- Math-----
-----

%Return Effective Moduli
[H_Top,ExBar_Top,EyBar_Top,NuxyBar_Top,GxyBar_Top,N_Top] =
EffectiveModuli(ThetaArray_Top,E1,E2,nul2,G12,h);
[H_Bot,ExBar_Bot,EyBar_Bot,NuxyBar_Bot,GxyBar_Bot,N_Bot] =
EffectiveModuli(ThetaArray_Bot,E1,E2,nul2,G12,h);
[H_Web,ExBar_Web,EyBar_Web,NuxyBar_Web,GxyBar_Web,N_Web] =
EffectiveModuli(ThetaArray_Web,E1,E2,nul2,G12,h);

%Find Moment of Inertia
if BEAM_TYPE == 1
    %Find Centroid w.r.t. y-axis
    ATop = Top_Flange_Width*Top_Flange_Thickness;
    yTop = Bottom_Flange_Thickness + Web_Height +
Top_Flange_Thickness/2;
    AWeb = Web_Height*Web_Thickness;
    yWeb = Bottom_Flange_Thickness + Web_Height/2;
    ABottom = Bottom_Flange_Width*Bottom_Flange_Thickness;
    yBottom = Bottom_Flange_Thickness/2;
    y_bar = (ATop*yTop + AWeb*yWeb +
ABottom*yBottom)/(ATop+AWeb+ABottom);
    %Find Iyy of each section
    IyyTop = Top_Flange_Width*Top_Flange_Thickness^3/12 +
ATop*(yTop-y_bar)^2;
    IyyBottom = Bottom_Flange_Width*Bottom_Flange_Thickness^3/12 +
ABottom*(yBottom-y_bar)^2;
    IyyWeb = Web_Thickness*Web_Height^3/12 + AWeb*(yWeb-y_bar)^2;
    %Calculate Total E*Iyy
    EI = ExBar_Top*IyyTop+ExBar_Bot*IyyBottom+ExBar_Web*IyyWeb;
    %Find Shear Area Ac
    Ac = AWeb;
elseif BEAM_TYPE == 2
    %Find Centroid w.r.t. y-axis
    ATop = Top_Flange_Width*Top_Flange_Thickness;
    yTop = Bottom_Flange_Thickness + Web_Height +
Top_Flange_Thickness/2;
    AWeb = 2*Web_Height*Web_Thickness;
    yWeb = Bottom_Flange_Thickness + Web_Height/2;
    ABottom = Bottom_Flange_Width*Bottom_Flange_Thickness;
    yBottom = Bottom_Flange_Thickness/2;

```

```

        y_bar = (ATop*yTop + AWeb*yWeb +
ABottom*yBottom) / (ATop+AWeb+ABottom);
        %Find Iyy of each section
        IyyTop = Top_Flange_Width*Top_Flange_Thickness^3/12 +
ATop*(yTop-y_bar)^2;
        IyyBottom = Bottom_Flange_Width*Bottom_Flange_Thickness^3/12 +
ABottom*(yBottom-y_bar)^2;
        IyyWeb = Web_Thickness*Web_Height^3/12 + AWeb*(yWeb-y_bar)^2;
        %Calculate Total Iyy
        EI = ExBar_Top*IyyTop+ExBar_Bot*IyyBottom+ExBar_Web*IyyWeb;
        %Find Shear Area Ac
        Ac = 2*AWeb;
    elseif BEAM_TYPE == 3
        %Find Iyy
        I = Box_Beam_Outer_Width*Box_Beam_Outer_Height^3/12-
(Box_Beam_Outer_Width-
2*Box_Beam_Vertical_Thickness)*(Box_Beam_Outer_Height-
2*Box_Beam_Horizontal_Thickness)^3/12;
        %Find Shear Area Ac
        ABox = Box_Beam_Outer_Width*Box_Beam_Outer_Height-
(Box_Beam_Outer_Width-
Box_Beam_Horizontal_Thickness)*(Box_Beam_Outer_Height-
Box_Beam_Vertical_Thickness);
        Ac = 20/47*ABox;
    end
%Beam Max Deflection for Simply Supported Beam with Distributed Load
    q_MLC_120_Entire_Bridge = q_MLC_120*L_MLC_120/L;
    Del_Max_MLC_120_Dist_Load =
5/384*q_MLC_120_Entire_Bridge*L^4/(EI)+1/8*q_MLC_120_Entire_Bridge*L^2/
(GxyBar_Web*Ac);
%Beam Max Deflection for Simply Supported Beam with Center Point Load
    Del_Max_MLC_120_Point_Load =
1/48*(q_MLC_120*L_MLC_120)*L^3/(EI)+1/4*(q_MLC_120*L_MLC_120)*L/(GxyBar_
_Web*Ac);
%Beam Deflection due to Mud Load
    Del_Max_Mud = 5/384*q_Mud*L^4/(EI)+1/8*q_Mud*L^2/(GxyBar*Ac);
%TOTAL DEFLECTIONS
    Del_Total_MLC_120_Dist_Load = Del_Max_MLC_120_Dist_Load +
Del_Max_Mud;
    Del_Total_MLC_120_Point_Load = Del_Max_MLC_120_Point_Load +
Del_Max_Mud;

%% -----Outputs-----
-----
fprintf(' Number of Layers = %g \n',N)
fprintf(' Laminate Thickness = %g mm \n',H*1e3)
fprintf(' ExBar = %g GPa \n',ExBar/1e9)
fprintf(' EyBar = %g GPa \n',EyBar/1e9)
fprintf(' NuxyBar = %g \n',NuxyBar)
fprintf(' GxyBar = %g GPa \n',GxyBar/1e9)
fprintf('The Maximum Central Displacement is %g m assuming the tank as
a distributed load \n',Del_Total_MLC_120_Dist_Load)
fprintf('The Maximum Central Displacement is %g m assuming the tank as
a point load \n',Del_Total_MLC_120_Point_Load)

```

```

fprintf('The observed experimental deflection is %g m
\n',convlength(11.825,'in','m'))
fprintf('The observed experimental deflection at overload (1.33xLoad)
is %g m \n',convlength(16.455,'in','m'))

function [H,ExBar,EyBar,NuxyBar,GxyBar,N] =
EffectiveModuli(ThetaArray,E1,E2,nu12,G12,h)
%returns effective moduli for a given laminate

N = length(ThetaArray);
[H,ZArray] = HowThick(ThetaArray,h);
QBarArray = cell(length(ThetaArray));
Q = ReducedStiffness(E1,nu12,E2,G12);
for i = 1:length(ThetaArray)
    QBarArray{i} = OffAxisStiffness(Q,ThetaArray(i));
end

%find abd and properties
[A,B,D,ABD,a,b,d,abd]=LaminateABD(N,QBarArray,ZArray);
ExBar = 1/(a(1,1)*H);
EyBar = 1/(a(2,2)*H);
NuxyBar = -a(1,2)/a(1,1);
GxyBar = 1/(a(3,3)*H);
End

function Q = ReducedStiffness(E1,nu12,E2,G12)
% ReducedStiffness calculates the plane stress reduced elastic
% stiffness matrix [Q] for a composite lamina.
%
% Syntax:
%   Q = ReducedStiffness(E1,nu12,E2,G12)
%
% Inputs:
%   E1 - Young's modulus in the 1-direction
%   nu12 - major Poisson's ratio
%   E2 - Young's modulus in the 2-direction
%   G12 - inplane shear modulus
%   Note 1 and 2 are the principal material directions.
%   Typically E1, E2 and G12 are specified in SI units of Pa.
%
% Output:
%   Q - 3x3 reduced stiffness matrix for a composite lamina
%
% Author: Senthil S. Vel, University of Maine
%
% See also ReducedCompliance, OffAxisStiffness, OffAxisCompliance.
%
% Calculate the minor Poisson's ratio using the reciprocal relations
nu21 = nu12*E2/E1;
%
% Evaluate the elements of the reduced stiffness matrix
Q11 = E1/(1-nu12*nu21);
Q12 = nu12*E2/(1-nu12*nu21);
Q22 = E2/(1-nu12*nu21);
Q66 = G12;

```

```

% Arrange the elements to form the reduced stiffness matrix [Q]
Q = [Q11 Q12 0;
     Q12 Q22 0;
     0 0 Q66];

End

function QBar = OffAxisStiffness(Q,Theta)
% OffAxisStiffness calculates the plane stress reduced elastic
% stiffness matrix [QBar] for an off-axis composite lamina.
%
% Syntax:
% QBar = OffAxisStiffness(Q,Theta)
%
% Inputs:
% Q - 3x3 plane-stress reduced stiffness matrix for a composite
lamina
% Theta - Angle in degrees from the x-axis to the 1-axis (CCW
positive)
%
% Output:
% QBar - 3x3 reduced stiffness matrix for an off-axis lamina
%
% Author: Senthil S. Vel, University of Maine
%
% See also ReducedCompliance, ReducedStiffness, OffAxisCompliance.

% Cosine and Sine of the angle
m = cosd(Theta);
n = sind(Theta);

% 2D reduced stiffness matrix (Q) values extraction
Q11 = Q(1,1); Q12 = Q(1,2); Q22 = Q(2,2); Q66 = Q(3,3);

% Calculate the off-axis stiffnesses QBar
QBar11 = Q11*m^4+2*(Q12+2*Q66)*m^2*n^2+Q22*n^4;
QBar12 = (Q11+Q22-4*Q66)*m^2*n^2+Q12*(m^4+n^4);
QBar16 = (Q11-Q12-2*Q66)*n*m^3+(Q12-Q22+2*Q66)*n^3*m;
QBar22 = Q11*n^4+2*(Q12+2*Q66)*n^2*m^2+Q22*m^4;
QBar26 = (Q11-Q12-2*Q66)*n^3*m+(Q12-Q22+2*Q66)*n*m^3;
QBar66 = (Q11+Q22-2*Q12-2*Q66)*n^2*m^2+Q66*(n^4+m^4);

% Assemble the QBar matrix
QBar =[QBar11 QBar12 QBar16;
       QBar12 QBar22 QBar26;
       QBar16 QBar26 QBar66];

end

function [A,B,D,ABD,a,b,d,abd]=LaminateABD(N,QBarArray,ZArray)
% LaminateABD computes the [A], [B], [D] and [ABD] matrices of a
laminate.

```



```

% In addition, it computes the [a], [b], [d] and [abd] matrices where
% [abd] is
% the inverse of [ABD].
%
% Syntax:
%   [A,B,D,ABD,a,b,d,abd] = LaminateABD(N,QBarArray,ZArray)
%
% Inputs:
%   N           - Number of layers in the laminate
%   QBarArray   - An array where QBarArray{k} is a 3x3 matrix of off-
axis
%               stiffnesses of the kth layer of the laminate
%   ZArray      - Array of interface z-coordinates of a laminate
%
% Output:
%   A   - [A] matrix (3x3)
%   B   - [B] matrix (3x3)
%   D   - [D] matrix (3x3)
%   ABD - [ABD] matrix (6x6)
%   a   - [a] matrix (3x3)
%   b   - [b] matrix (3x3)
%   d   - [d] matrix (3x3)
%   abd - [abd] matrix, inverse of ABD (6x6)
%
% Author: Senthil S. Vel, University of Maine
%
% See also LaminateStrainsXY, LaminateStressesXY,
LaminateEngineeringProperties.

% Initialize the A, B and D matrices
A=zeros(3,3);
B=zeros(3,3);
D=zeros(3,3);

% Perform layer by layer summation to obtain the A, B and D matrices
for k = 1:N
    A = A + (ZArray(k+1)-ZArray(k))*QBarArray{k};
    B = B + (1/2)*((ZArray(k+1))^2-(ZArray(k))^2)*QBarArray{k};
    D = D + (1/3)*((ZArray(k+1))^3-(ZArray(k))^3)*QBarArray{k};
end

% Arrange the A, B and D into a 6x6 ABD matrix
ABD = [A B; B D];

% Find the inverse of the ABD matrix
abd = inv(ABD);
a = abd(1:3,1:3);
b = abd(1:3,4:6);
c = abd(4:6,1:3);
d = abd(4:6,4:6);

end

function [H,ZArray] = HowThick(ThetaArray,h)
%returns z locations and the overall thickness

```

```
H = length(ThetaArray)*h;
ZArray = linspace(-H/2,H/2,length(ThetaArray)+1);
End

function [Output] = MakeSymmetric(Input)
%This function makes a symmetric laminate
n = length(Input);
Output = zeros(2*n,1);
for i = 1:n
    Output(i,1) = Input(i);
    Output(2*n+1-i,1) = Input(i);
end
end
```

BIOGRAPHY OF THE AUTHOR

Andrew R. Moran was born in Lewiston, Maine. He was raised in Randolph, Maine and graduated third in his class from Gardiner Area High School. He attended the University of Maine (UMaine) and graduated with a Bachelor's of Science in Mechanical Engineering and a minor in Technical Theatre in 2019. Upon graduation he entered the graduate program in Mechanical Engineering at UMaine and focused his master's research on composite structures at the Advanced Structure and Composites Center (ASCC).

Andrew is a lover of the performing arts. He has participated in many academic and professional productions, serving in many roles including backstage technician and lighting designer.

Andrew is a candidate for the Masters of Science degree in Mechanical Engineering from the University of Maine in May 2022.